UCRL 9288

UNIVERSITY OF CALIFORNIA

Ernest O. Lawrence

Radiation Laboratory

ANTIPROTON-NUCLEON CROSS SECTIONS FROM 0.5 to 1.0 Bev

TWO-WEEK LOAN COPY

This is a Library Circulating Copy which may be borrowed for two weeks. For a personal retention copy, call Tech. Info. Division, Ext. 5545

DISCLAIMER

This document was prepared as an account of work sponsored by the United States Government. While this document is believed to contain correct information, neither the United States Government nor any agency thereof, nor the Regents of the University of California, nor any of their employees, makes any warranty, express or implied, or assumes any legal responsibility for the accuracy, completeness, or usefulness of any information, apparatus, product, or process disclosed, or represents that its use would not infringe privately owned rights. Reference herein to any specific commercial product, process, or service by its trade name, trademark, manufacturer, or otherwise, does not necessarily constitute or imply its endorsement, recommendation, or favoring by the United States Government or any agency thereof, or the Regents of the University of California. The views and opinions of authors expressed herein do not necessarily state or reflect those of the United States Government or any agency thereof or the Regents of the University of California.

UCRL-9288
UC-34 Physics and Mathematics
TID-4500 (15th Ed.)

UNIVERSITY OF CALIFORNIA

Lawrence Radiation Laboratory
Berkeley, California

Contract No. W-7405-eng-48

ANTIPROTON-NUCLEON CROSS SECTIONS FROM 0.5 to 1.0 Bev

Tommy Elioff

(Ph. D. Thesis)

July 18, 1960

Printed in USA. Price $2.00. Available from the
Office of Technical Services
U. S. Department of Commerce
Washington 25, D.C.

ANTIPROTON-NUCLEON CROSS SECTIONS FROM 0.5 to 1.0 Bev

Contents

Abstract 4

I. Introduction 6

II. Apparatus . . . . . .

A. Antiproton Beams 10

B. Beam Counters 15

C. Apparatus for the Detection of Antiproton Interactions 24

1. Hydrogen Target 24

2. Interaction Detectors 28

D. Electronics and Antiproton Identification 29

III. Procedure

A. Data Accumulation. 33

B. Classification of Antiproton Interaction Events . . 34

C. Experimental Checks

1. Proton-Proton Cross Sections 36

2. Tests for Accidental Coincidences 37

IV. Antiproton Production

A. Production in Hydrogen 38

B. Production in Carbon 39

V. Antiproton-Proton Cross Sections

A. Calculations and Results 48

B. Corrections and Uncertainties 50

C. Discussion of Results 52

1. General Features 52

2. The Inelastic Process 55

3. Angular Distribution of Elastic Scattering . . 57

D. Conclusion 65

VI. Determination of Antiproton-Neutron Cross Sections
A. Discussion 68
B. Antiproton-Deuteron Cross Section Results . . . 69
C. The "Eclipse" Effect and Antiproton-Neutron Cross Sections 73
D. Conclusion 79
Acknowledgments 82
Appendix: Antiproton Cross Section Formulas 83
References 87

ANTIPROTON-NUCLEON CROSS SECTIONS FROM 0.5 to 1.0 Bev

Tommy Elioff

Lawrence Radiation Laboratory
University of California
Berkeley, California

July 18, 1960

ABSTRACT

Antiproton-production and nucleon-interaction cross sections were determined for antiprotons in the energy range 0.5 to 1.0 Bev. The production of antiprotons in hydrogen by 6.0-Bev incident protons was investigated by observing the number of antiprotons produced in polyethylene and carbon targets within the Bevatron. The antiprotons were identified by a system of scintillation and velocity-selecting Cherenkov counters. The results indicated that antiproton production in hydrogen is negligible compared with production in carbon. The excitation function and momentum distribution were recorded for antiproton production in carbon and compared with statistical-model expectations.

After the antiprotons made their exit from the Bevatron, they were directed by a system of bending and focusing magnets to a liquid hydrogen target. An array of plastic scintillation counters, which nearly completely surrounded the hydrogen target, was used to determine the antiproton-proton total, elastic, inelastic, and charge-exchange cross sections at five energies in the above energy range. It was found that the total cross sections are everywhere much larger than the nucleon-nucleon cross sections for comparable energies. Near 500 Mev the total antiproton-proton cross section is about 120 mb, and it slowly decreases to 100 mb near 1 Bev. The inelastic cross section,

which is principally due to the annihilation process, represents nearly 2/3 of the total cross section. The elastic scattering distribution is highly peaked in the forward direction and can be fitted by optical-model analysis.

The total and partial cross sections were also determined for the collisions of antiprotons with deuterons. The antiproton-deuteron cross sections were found to be approximately 1.8 times the antiproton-proton cross sections. Corrections were made for the shielding of nucleons within the deuteron so that we could observe the antiproton-neutron interaction. The results indicate that the antiproton-proton and antiproton-neutron cross sections are very nearly equal and that they satisfy the relations governed by charge independence.

I. INTRODUCTION

As antiprotons are now included in the observed spectrum of subatomic particles, a knowledge of their interaction with nucleons is essential for a complete description of nuclear forces. To this end, a considerable amount of experimental data on the antiproton-proton interaction has already been obtained even though the discovery of the antiproton was relatively recent[1] and in spite of the fact that antiproton-production cross sections are relatively small at the Bevatron energy. Complete surveys of the previous experimental data as well as existing theoretical implications, which chiefly pertain to antiprotons having energies only up to several hundred Mev, may be found in the reports of Segrè[2, 3] and Chamberlain.[4]

The fundamental purpose of this experiment was to continue the investigation of the antiproton-proton ($\bar{p}$-p) cross sections at higher antiproton kinetic energies--specifically from 534 to 1068 Mev. By cross sections we mean the total (σ_t), the elastic (σ_e), the inelastic (σ_i), and the charge-exchange (σ_c) cross sections. What is called inelastic cross section here is synonymous with annihilation cross section for antiproton kinetic energies below the threshold (288 Mev) for pion production. Above 288 Mev, the inelastic cross section includes both annihilation and inelastic scattering or pion production.

Most of the prior antiproton experiments utilized antiprotons having kinetic energies from 0 to 300 Mev. For this energy interval, the characteristic features of the $\bar{p}$-p interaction are briefly:

(a) The $\bar{p}$-p cross sections are several times the nucleon-nucleon cross sections of corresponding energy.

(b) The annihilation process constitutes a large fraction of the $\bar{p}$-p total cross section, whereas there is no inelastic process in the nucleon-nucleon system.

Although these features were at first thought unusual in contrast to the nucleon-nucleon data, the calculations of Ball and Chew[5] based on the conventional Yukawa pion-exchange mechanism showed the result to be expected. The predictions of the Ball-Chew model are in excellent agreement with the experimental data from 50 to 200 Mev. The calculations by Ball and Chew are not applicable above 250 Mev; however, a model of the $\bar{p}$-p interaction advanced by Koba and Takeda[6] is applicable at higher energies and it is of interest to compare the results of this experiment with their predictions.

It should be mentioned that the determination of the $\bar{p}$-n (also $\bar{n}$-p) cross section is just as important as the $\bar{p}$-p. Thus an additional purpose of this experiment was to measure $\bar{p}$-d (antiproton-deuteron) cross sections and thus obtain the $\bar{p}$-n cross sections by a subtraction procedure between $\bar{p}$-d and $\bar{p}$-p data. A comparison of the $\bar{p}$-p and $\bar{p}$-n results then reveals the amount of interaction in the two possible isotopic spin states of the nucleon-antinucleon system. Only one experimental $\bar{p}$-n cross section (at 450 Mev)[7] was known prior to this experiment.

A particularly important reason for exploring the high-energy $\bar{p}$-p cross sections was the hope of explaining an apparent contradiction in two previous experiments near 500 Mev. The experiment of Chamberlain et al.[7] measured the total $\bar{p}$-p cross section in poor geometry and also the inelastic cross section, while the experiment of Cork et al.[8] measured the total cross section in good geometry. If one believed the results of both experiments, one was led to the conclusion that there was no diffraction scattering, whereas the inelastic cross section was very nearly the total cross section. In sharp contrast, the subsequently determined low-energy results (0 to 200 Mev) displayed a forward diffraction peak, and one found $\sigma_e \approx \sigma_i$. Up to the time of this experiment the situation remained a puzzle and led some theorists to search for unusual potentials that might describe the interaction near 500 Mev.[9]

It is possible that some idea of nucleon structure may result from a study of the $\bar{p}$-p interaction at high energies. If one assumes that a physical nucleon is composed of a core region surrounded by a virtual pion cloud, then the annihilation process presumably will take place whenever the core regions of nucleon and antinucleon come in contact. Thus, because of this direct relation of the annihilation process to the core region, one might expect the annihilation cross section to reveal the core size. Chew has pointed out that this is not possible at low energies because the pion potential is very effective in enhancing the annihilation cross section by deflecting the antiproton in toward the core region;[10] however, it is conceivable that at some high energy the effect of the pion cloud may become negligible and here the core radius may be determined.

The antiproton energy range (534 to 1068 Mev) of this experiment was selected for the reasons already mentioned, and in addition because it appeared to be the optimum energy interval in which to explore antiproton-production cross sections. Antiproton production in hydrogen and carbon were of particular interest here. When 6-Bev protons bombard carbon, the proton-nucleon processes

$$p + p \rightarrow \bar{p} + p + p + p, \tag{1}$$

$$p + n \rightarrow \bar{p} + p + p + n \tag{2}$$

are expected to be of importance. Of course production in hydrogen would involve (1) only. Hydrogen is the more desirable element because the fundamental process is not obscured by the presence of other nucleons, as in carbon. A knowledge of the exact threshold for antiproton production would be useful in determining if the above nucleon-nucleon processes are important or if some other processes such as pion-nucleon collisions are also present. Additional features such as the angular and momentum distributions of the produced antiprotons would be expected to shed some light on whether one can predict relative production rates by statistical-model considerations. More precise theoretical results are lacking for high-energy processes with multiparticle final states such as the ones above.

Antiproton production in hydrogen was of interest because of the prior results of another experiment[11,12] in which the production of approx 500-Mev antiprotons was found to be greater when the target material was a free proton than when it was an average nucleon in carbon. Statistical-model predictions indicated that the reverse should be true largely because of the extra Fermi energy of the nucleons in carbon. In section IV the results of this experiment on antiproton production in hydrogen are given; the results are in disagreement with those of Reference 12. The experimental excitation function and some information on the momentum and angular distributions of antiprotons produced from carbon are also presented and compared with statistical-model predications as well as the experimental results of others.

In Section V additional details of the $\bar{p}$-p inelastic process are analyzed. An upper limit is set to the amount of inelastic scattering that is included with the annihilation in the total inelastic cross section. The $\bar{p}$-p elastic scattering is prominent in the forward direction. The angular distributions at forward angles are given and compared with optical-model expectations.

II. APPARATUS

A. Antiproton Beams

As the threshold for antiproton production from stationary nucleons is 5.62 Bev, one finds at the Bevatron that antiprotons are rare particles in comparison with the copiously produced pions. Consequently one of the principal experimental tasks is to form a relatively pure antiproton beam. In a counter experiment such as this, the antiproton beam is an electronically selected component of a momentum-analyzed beam of negatively charged particles of all kinds--predominantly pions. The characteristics of the magnetic channel for momentum analysis are discussed in the following paragraphs, and the counters used for the electronic selection are described in Section B.

The magnetic channel used here was similar to those of previous experiments.[12, 13] This system differed in that it was physically longer and the momentum spread of particles traversing the channel was slightly larger. In general the elements comprising the channel were arranged so that higher antiproton energies (up to 1100 Mev) were attainable. Specifically the five energies utilized here were 534, 700, 816, 934, and 1068 Mev.

A schematic diagram of the experimental area is shown in Fig. 1 and its principal components are identified in Table I. The Bevatron internal proton beam strikes either a carbon or a polyethylene target schematically represented by T. Normally, to dispose of radio-frequency structure, the Bevatron internal beam first encounters a primary target consisting of several nylon strings. The energy loss resulting from repeated passage through these fibers causes the protons to spiral in toward target T. By controlling the manner in which the circulating beam strikes the strings, we could obtain a more uniform internal beam with a duration of 75 to 100 milliseconds. This procedure for beam spill was used for the major part of the experiment; however, certain modifications mentioned in Section IV were made in order to study antiproton production.

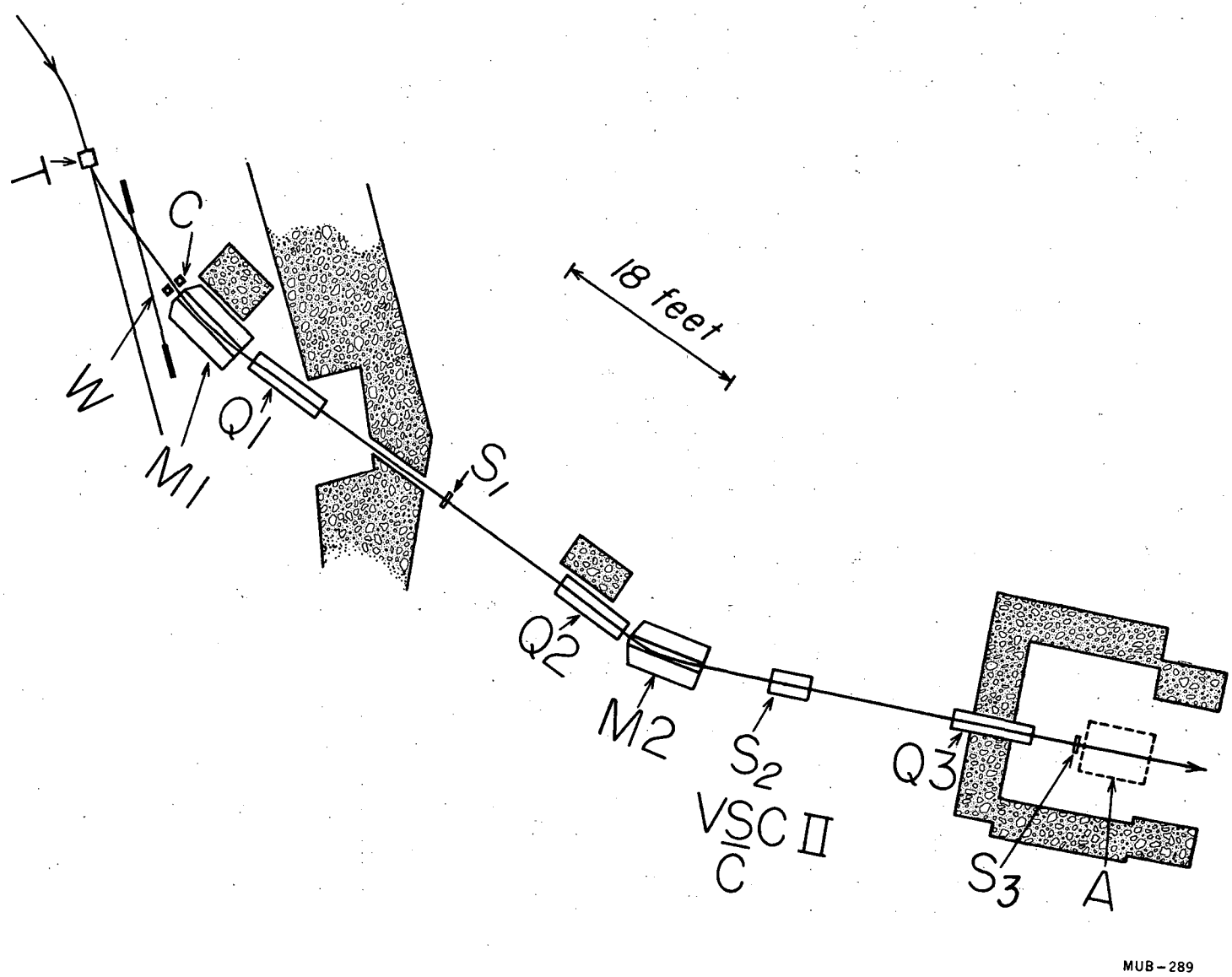

Fig. 1. Schematic view of the Bevatron experimental area. Components are identified in Table I.

Table I

Experimental components of Fig. 1	
Symbol	Component description
T	Bevatron target area
W	Thin window of Bevatron vacuum system (0.020-in. Al)
C	Brass collimator, 6 in. in diam by 8 in. thick
M1, M2	60-in.-long deflection magnets with 12-by 7-in. aperture (θ_{M1} = 17 deg, θ_{M2} = 25 deg)
Q1, Q2, Q3	Sets of quadrupole focusing magnets of 8-in. aperture
S_1	Plastic scintillation counter 3-1/2 in. in diam. by 1/4 in. thick
S_2	Plastic scintillation counter 3-1/16 in. in diam. by 1/4 in. thick
VSC II	Antiproton narrow-band velocity-selecting Cherenkov counter which utilizes cyclohexene radiator ($n = 1.46$, $\rho = 0.8$ g/ml) 3-1/4 in. in diam. and 4.7 in. long. The velocity resolution is $\Delta\beta = 0.03$ in the range $0.95 > \beta > 0.70$.
$\bar{C}$	Meson Cherenkov counter which utilizes the same radiator as VSC II but views only Cherenkov light that is totally internally reflected, i.e., for $\beta > 0.95$.

Table I (continued)

Symbol	Component description
S_3	Plastic scintillation counter 5 in. in diam. by 3/8 in. thick
A	Area for hydrogen target and final counter system

To obtain $\bar{p}$ beams of the five desired energies through our fixed system of magnets, we utilized several target positions in the region represented by T (Fig. 1). This was to allow observation of the antiprotons at small angles from the Bevatron beam direction. Selection of these positions was facilitated by the use of the IBM 650 program "Ethelbert", which computes the path of charged particles through the Bevatron magnetic field. Three positions were selected (at each position a carbon and a polyethylene target were used alternately) for which the magnetic channel could select antiprotons in the desired energy range with angles of emission 0 to 4 deg with respect to the Bevatron internal-beam direction. Small angles of emission were desirable for maximum antiproton intensity. It was then also possible to obtain an external beam of a given momentum at three different angles of emission, two of which were greater than 4 deg. This feature allowed us to obtain a crude angular distribution for the produced antiprotons.

After the antiprotons were produced in the selected target (T), they were deflected away from the Bevatron by the Bevatron magnetic field and magnet M1; subsequently Q1 focused them in the region S_1. Q2 refocused the antiprotons in the region S2. M2 served to direct the antiprotons of the desired momentum along the beam line toward Q3 and to cancel the momentum dispersion caused by the Bevatron field and M1. Finally the antiprotons entered the aperture of Q3, which brought them to the final focal point F3 (see Fig. 6) located in area A of Fig. 1.

To reduce losses due to air scattering, the beam traversed a helium atmosphere from its exit at W to the region A at the terminal end of the channel. The momentum spread, $\Delta p/p$, of the system described above was ±3%. At 10 pulses per minute for a normal Bevatron beam of approx 7×10^{10} protons per pulse, approximately 10^5 pions and 5 antiprotons traversed the magnetic channel during each Bevatron pulse. More precise production rates are given in Section IV.

In order to quickly set up the antiproton beams with assurance that all magnets were properly aligned and to be certain that all magnet currents were correctly set when alternating between various Bevatron targets and different antiproton momenta, we used a device called the Beam Profile Indicator to immediately observe the beam-intensity distribution at any point in the magnetic channel. This device is described in more detail elsewhere.[14]

Basically the Indicator is a row of 21 plastic scintillator elements. Each scintillator has a 1-cm^2 area to the beam direction and is viewed by a 1P21 photomultiplier tube. Transistor circuits amplify and integrate the output of each tube. When particles traverse the scintillators, the accumulated charge from each element is read out in sequence and displayed on an oscilloscope where the beam intensity pattern appears as a histogram. A typical beam pattern is shown in Fig. 2. The device can be momentarily inserted at any point in the beam and can also be rotated about the beam direction to get the profile in any plane through the beam direction.

B. Beam Counters

The magnetic channel that formed a momentum-analyzed beam of negatively charged particles has been described in Section A. In this section we describe the counters used to select the antiprotons from other particles of different mass in the beam.

At momenta at which the velocity of pions is quite different from the velocity of antiprotons, one can distinguish the antiprotons entirely by time-of-flight techniques. However, at the energies involved in this experiment, at which the velocity of the antiprotons approaches that of the pions, we found that a combination of time-of-flight technique with velocity-selecting Cherenkov counters provided the optimum detection efficiency. Three scintillation counters, S_1, S_2, and S_3, were used for the time-of-flight measurement. The positions of these counters

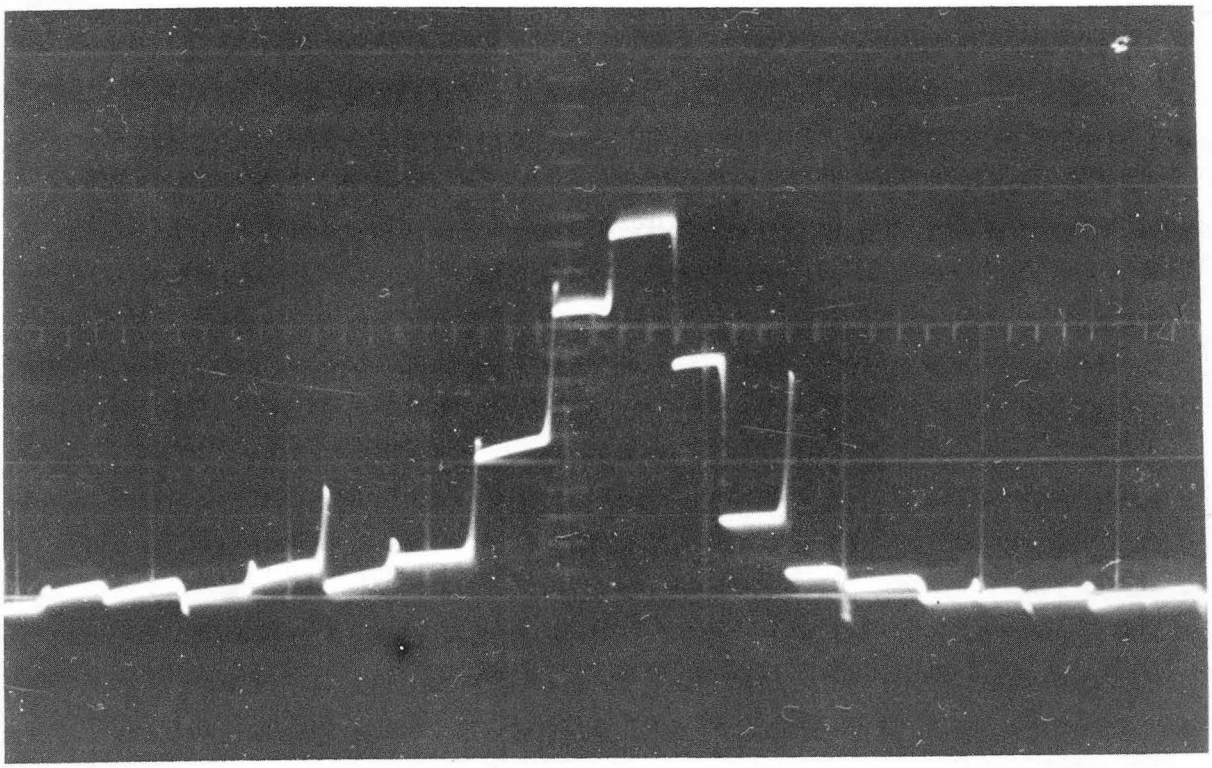

ZN-2553

Fig. 2. Oscilloscope photograph of beam-intensity pattern behind hydrogen target. Each step in the histogram represents 1 cm in the vertical plane.

along the beam are shown in Fig. 1 and their dimensions are given in Table I. In order for the pulses from the three scintillators to have fast rise times each scintillator was viewed by an RCA 7264 photomultiplier tube, which has a fully rounded photocathode. Experimental delay curves determined at normal beam intensities showed that the time-of-flight measurement rejected only 99% of the pions. The effective discrimination against the remaining pions was obtained by the use of the velocity-selecting Cherenkov counter, VSC II, and the pion Cherenkov counter $\bar{C}$.

VSC II is in principle exactly like the original velocity-selecting Cherenkov counter designed by Wiegand and Chamberlain.[15,16] The particular model used here, VSC II, is almost twice as large as the earlier version, which was designed for use in beams utilizing 4-in.-diameter quadrupole magnets, whereas here 8-in. quadrupoles are used. An additional modification is in the use of three RCA 7046 photomultiplier tubes. A schematic diagram of VSC II and $\bar{C}$ is given in Fig. 3.

The VSC II counter functions as follows: When a charged particle of velocity v traverses a medium which has an index of refraction n, Cherenkov light is emitted at an angle θ with respect to the particle direction, where θ is given by

$$\cos\theta = \frac{c}{nv} = \frac{1}{n\beta}, \tag{3}$$

and c is the velocity of light. As seen in Fig. 3, the refracted light leaves the radiator at angle θ', whereafter it is guided by the cylindrical mirror and the three plane mirrors (arranged in a triangle) to the photomultiplier tubes. The plane mirrors merely serve to remove the tubes from the beam. Light emitted by a particle of given β reaches the photomultipliers only when the radiator, cylindrical mirror, and photomultipliers have the proper separation governed by the angle θ'.

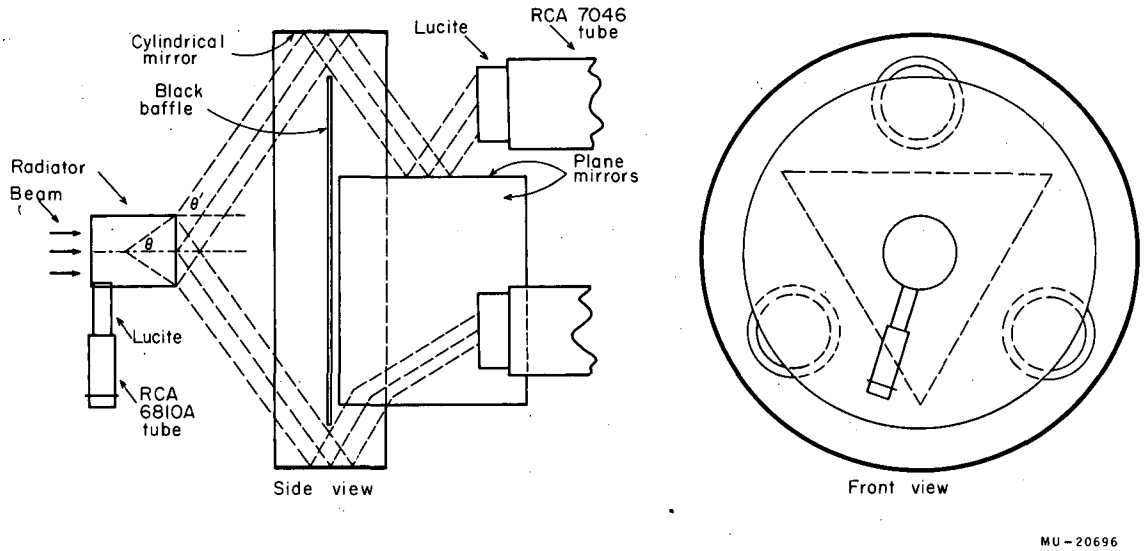

Fig. 3. Schematic diagram of the VSC II and $\overline{C}$ counters.

These components slide on rails so that the counter can be easily adjusted for different velocities. The entire instrument is contained in a lighttight black box. The light from particles slower or faster than the desired velocity misses the cylindrical mirror and is absorbed by the baffle or the outer black box. Accidental counts are minimized by the requirement that all three photomultipliers give an output in coincidence.

Figure 4 shows the efficiency for two particular velocity settings (indicated by the arrows) of the VSC II corresponding to antiprotons having momenta of 1200 Mev/c and 1640 Mev/c. The curves were actually obtained by sending protons of different velocities down the magnetic channel. The efficiency is defined as the ratio of the fourfold coincidence $S_1 S_2 S_3$ VSC II to the threefold coincidence of $S_1 S_2 S_3$.

The VSC II radiator material was cyclohexene. The liquid was contained in a thin-walled lucite cylinder 4.7 in. long and 3.25 in. in diameter. Cyclohexene ($CH{:}CH(CH_2)_3CH_2$) was chosen because of its low density, 0.81 g/cc, its inability to scintillate, and chiefly because its refractive index (n = 1.46) was optimum for use in both VSC II and $\overline{C}$. The cyclohexene index 1.46 corresponds to a wave length of 4250A. This is an average effective wave length estimated from the response of the RCA 7046 tube to the Cherenkov radiation spectrum that is transmitted through the lucite container of the radiator and the lucite light pipe on the face of the 7046 tube. As shown in Fig. 4, the calculated settings agree with the experimental settings determined by protons.

We now turn to the other reason for the use of index 1.46, i.e., the $\overline{C}$ counter. Actually VSC II and $\overline{C}$ are two independent counters which utilize the same Cherenkov radiator. VSC II is used to detect antiprotons (or protons) of a selected velocity. $\overline{C}$ is used here specifically to count pions.

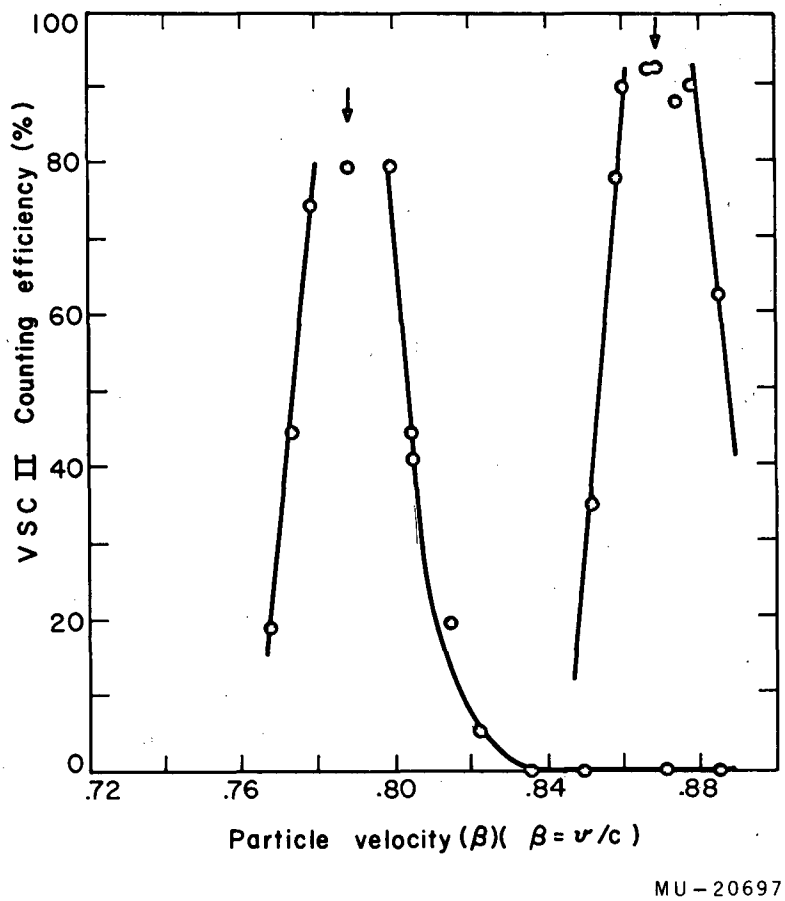

Fig. 4. Efficiency of the velocity-selecting-Cherenkov counter VSC II as a function of velocity. For two particular velocity settings of the counter corresponding to antiproton momenta of 1200 and 1640 Mev/c (indicated by the arrows), protons of various velocities (indicated by the experimental points) were sent through the counter. The resulting curves show the resolution and efficiency for the two desired velocity settings.

To be more explicit, it is first to be noted that owing to the mobility of the VSC II mirrors and tubes, there is a certain degree of freedom in the choice of the index of refraction of the radiator. One can easily see from Eq. (3) and Snell's Law that for an index $n > \sqrt{2}$, there is some velocity β' for which the Cherenkov light is totally internally reflected within the radiator. In this experiment it was desired to count antiprotons in the velocity range $0.7 \lesssim \beta \lesssim 0.9$, while the corresponding mesons of the same momenta have $\beta \gtrsim 0.998$. Therefore if $n = 1.46$ is chosen, we have $\beta' = 0.95$. This means that total internal reflection occurs for the Cherenkov radiation emitted by the pions and this light is trapped within the radiator. In order to vent this pion light and at the same time accept negligible light from the antiprotons, a lucite light pipe of cross section of 1 in.^{2} was put in optical contact near the front end of the radiator and coupled to another photomultiplier tube. The setup is displayed in Fig. 3. Most of the light from the pions, perhaps after several reflections around the radiator, eventually reaches the 6810A photomultiplier tube. This is the $\overline{C}$ pion counter.

Figure 5 presents a delay curve taken with scintillation counters, S_1, S_2, and S_3 delayed for pions and with $\overline{C}$ in anticoincidence with S_1, S_2, S_3. This curve shows that $\overline{C}$ is 99.985% efficient in detecting pions and thus, since it is used in anticoincidence, is able to reject all but 0.015% of accidental pions that might count as antiprotons. The various counter efficiencies are given in Table II.

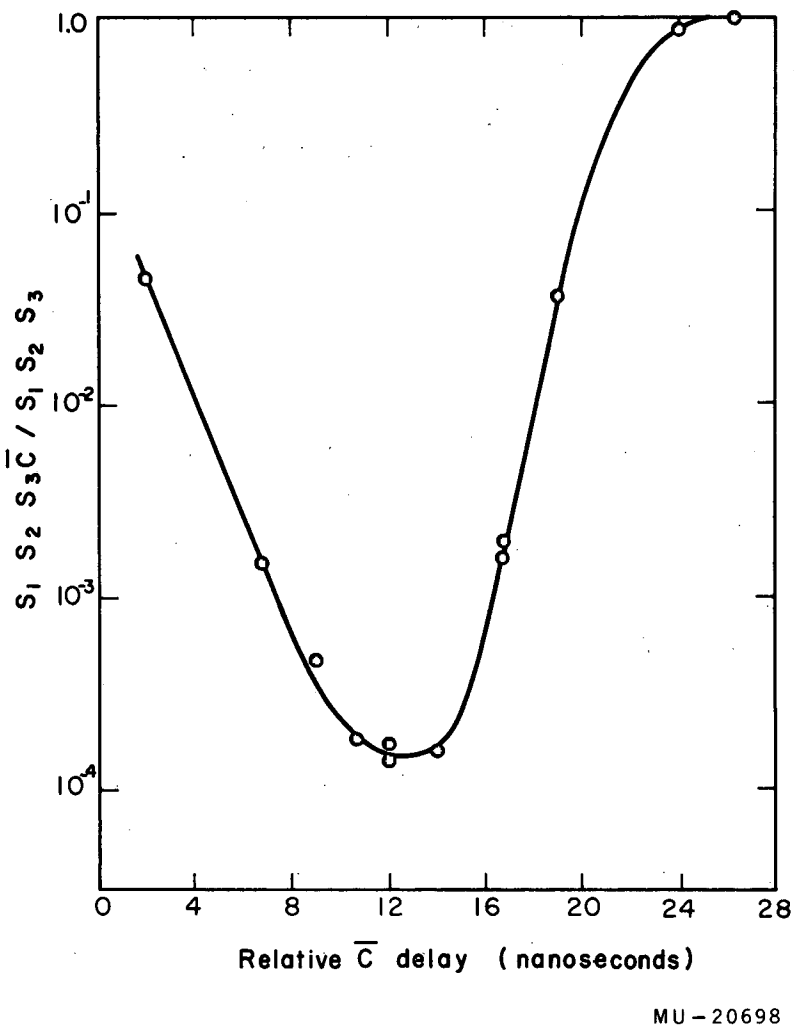

Fig. 5. Pion-rejection efficiency of the $\bar{C}$ counter when used in anticoincidence with scintillation counters S_1, S_2, and S_3.

Table II

Beam counter efficiencies		
Counters	Antiproton detection efficiency (%)	Pion detection efficiency(%)
S_1	100	100
S_2	100	100
S_3	100	100
$S_1S_2S_3$ coincidence (delayed for $\bar{p}$)	100	2
VSC II $\vec{p}_{\bar{p}} = 1200$ Mev/c	80	1
VSC II $\vec{p}_{\bar{p}} = 1640$ Mev/c	92.5	1
$\bar{C}$	≈ 0	99.985
$S_1S_2S_3$VSC II coincidence with $\bar{C}$ anticoincidence (all delayed for $\bar{p}$)	80 to 92.5	$\sim 13\times10^{-6}$

C. Apparatus for the Detection of Antiproton Interactions

This apparatus refers to the hydrogen (and deuterium) target and the final counter assembly, which were used to measure the $\bar{p}$-p and $\bar{p}$-d cross sections. The counter assembly consists of 27 scintillation counters which approximate a 4π geometry about the hydrogen target. The arrangement is represented in Figs. 6, 7, and 8.

1. Hydrogen Target

The schematic diagram in Fig. 6 shows a portion of the target assembly in relation to the surrounding counter system. Although it is not shown in the figure, a reservoir that can be filled with either hydrogen or deuterium is connected directly to the target container (A). A liquid hydrogen jacket partially surrounded this reservoir when deuterium was used; it served to condense the deuterium, which was maintained in a closed system. When hydrogen was used as the target material, the deuterium was removed from the entire system and liquid hydrogen was introduced into the reservoir formerly used for deuterium. The target flask (A) is a stainless steel cylinder 12 in. long and 6 in. in diameter with 0.008-in. walls, except for the beam entrance window, which is 0.010-inch Mylar. In the evacuated region around (A) is a 0.003-in. copper heat shield (C). The outer vacuum wall at the exit end (B) is a 0.035-in. -thick aluminum dome, which allowed particles leaving the target at large angles to avoid the heavier target structure. The entrance window of the vacuum system was 0.010-in. Mylar.

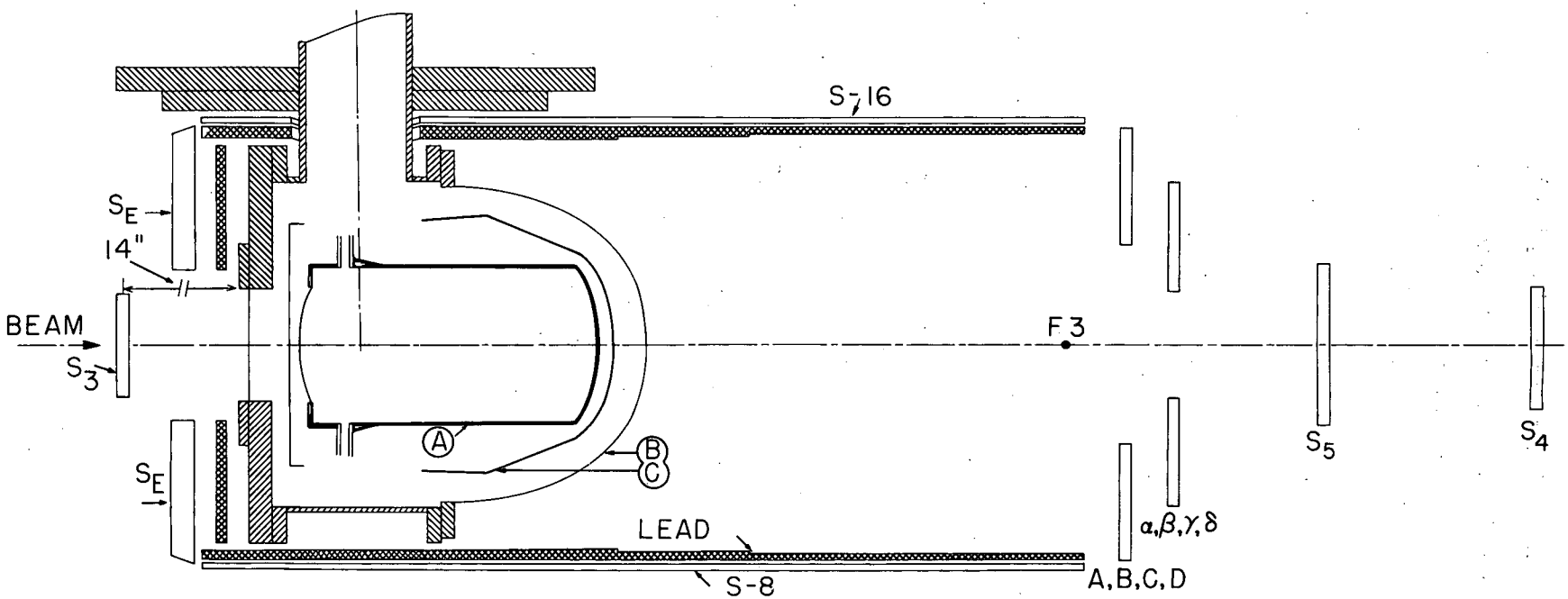

MUB-286

Fig. 6. Side view of target and counter system. For clarity the figure is not drawn precisely to scale. The target container (A) is a stainles steel cylinder 12 in. long and 6 in. in diameter, which could be filled with liquid hydrogen or deuterium. Sixteen scintillation counters, S-1 through S-16, cylindrically surround the target. Counters A, B, C, D, α, β, γ, δ, S_4, S_5 are shown more explicitly in the next figure. The lead between the target and the scintillators is removable.

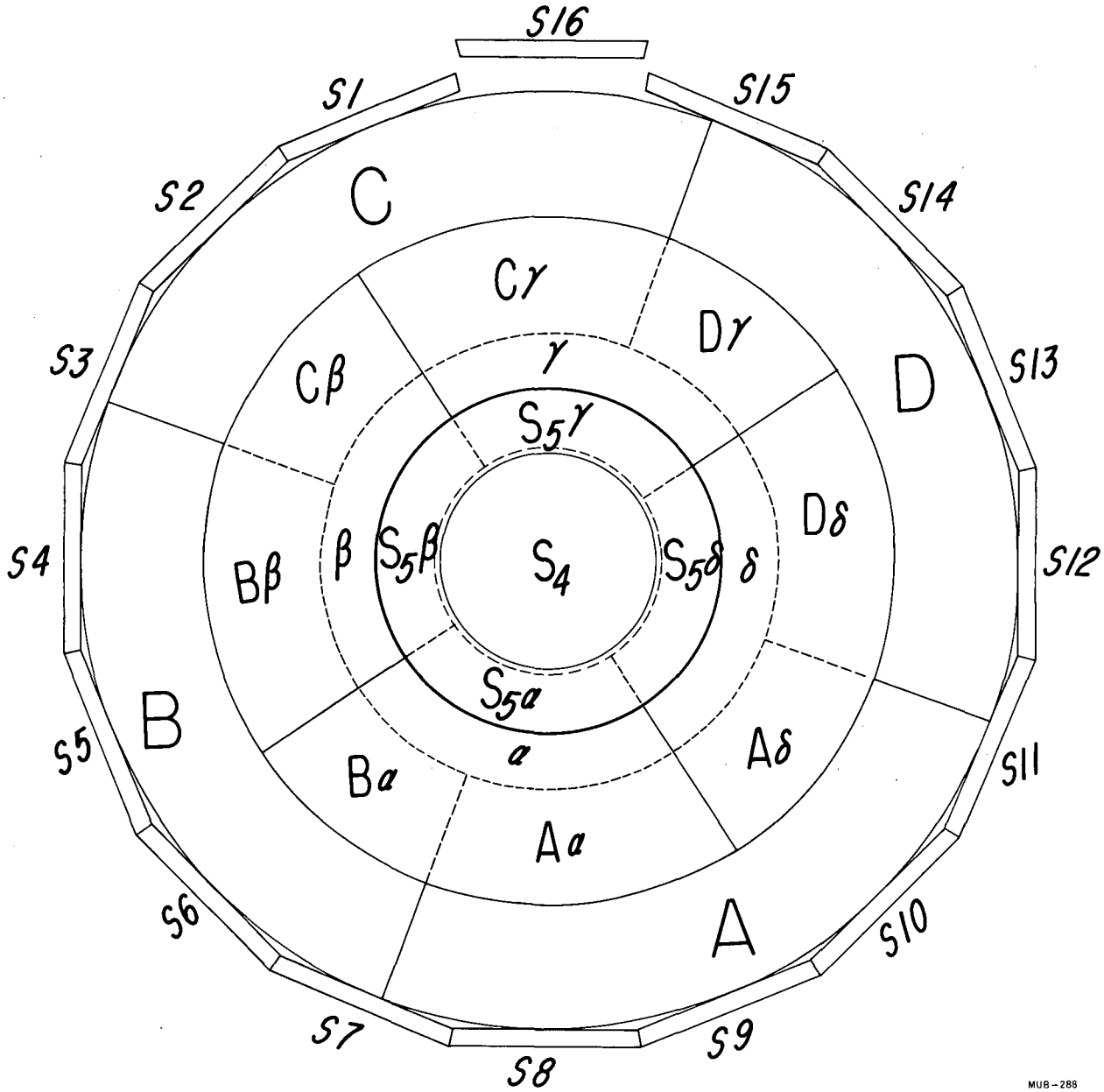

Fig. 7. Schematic view from the beam-exit end of the counter system. Counters A, B, C, D, α, β, γ, δ, S_4 and S_5 and their overlapping regions are displayed as well as the end view of counters S-1 through S-16.

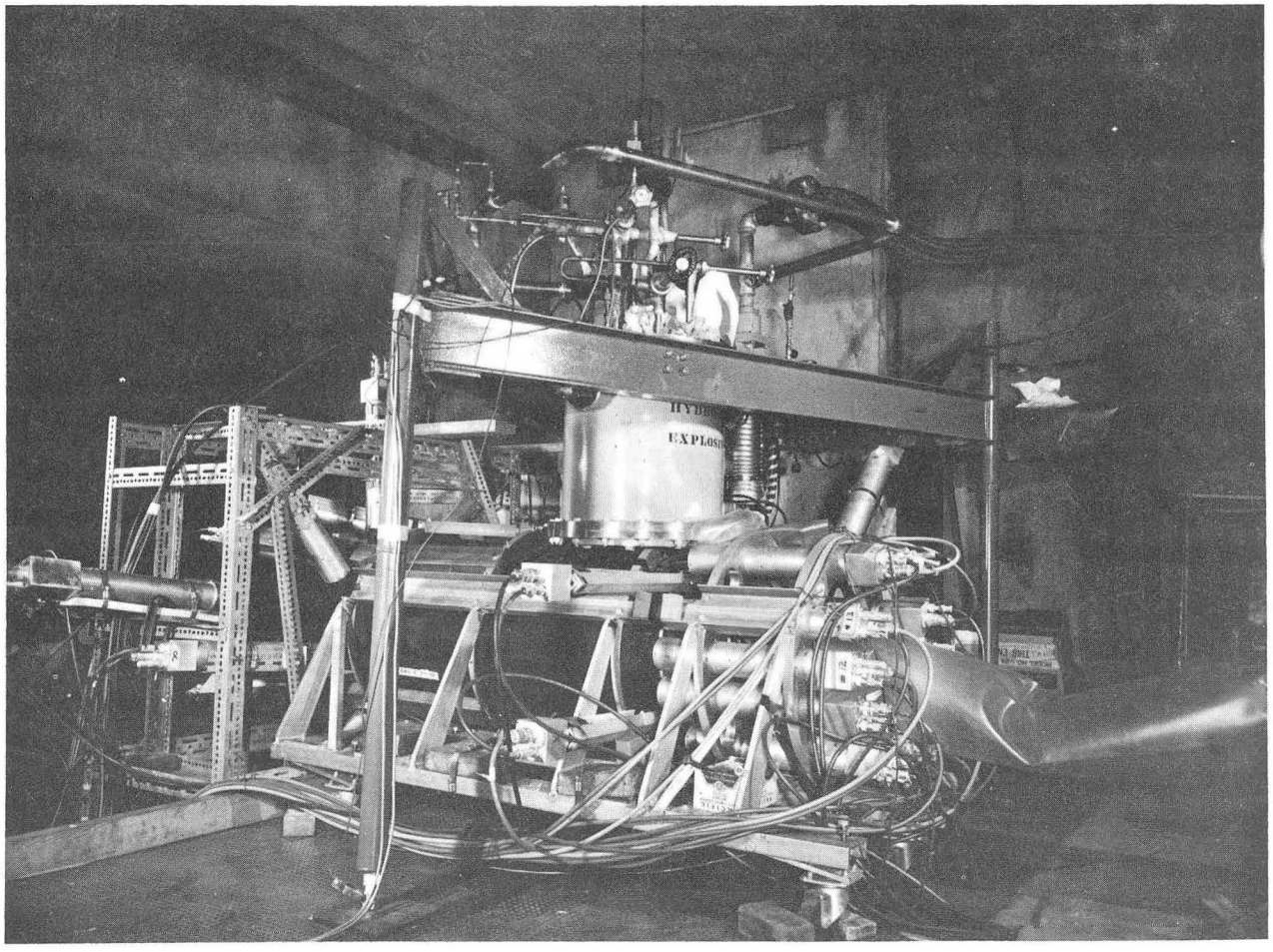

ZN-2554

Fig. 8. The antiproton-interaction detection system.

2. Interaction Detectors

The counter system surrounding the target was designed to distinguish between the various antiproton interaction processes. The fundamental idea is that the surrounding scintillators count all outgoing charged particles resulting from incident antiprotons on the hydrogen, whether they be antiprotons or the products of antiproton interactions within the target. A method similar to this was first used by Coombes et al.[17] to obtain $\bar{p}$-p cross sections at lower energies.

The particular arrangement of the counters is shown in Figs. 6 and 7. Sixteen counters, designated S-1, S-2, ··· S-16, encircle the target like the staves of a barrel; each is 38 by 4.1 by 0.375 in. Counters $\alpha, \beta, \gamma, \delta$, A, B, C, and D form concentric rings in the forward direction when viewed from the target; each ring has four azimuthal divisions. The projected arrangement is most clearly seen in Fig. 7. S_4 and S_5 are good-geometry counters used for total-cross-section measurements. Most of the above counters were made of 0.375-in.-thick plastic scintillators (97% polystyrene, 3% terphenyl, and 0.03% terphenyl butadiene), which were viewed by RCA 6810A photomultipliers. An exception to the above was the backup counter E, which was 1.0 in. thick and viewed by four 6810A tubes. The counters S_4 and S_5, which were used in coincidence with S_1, S_2, and S_3 for electronic cross-section measurements, also differed in that RCA 7264 tubes were used.

Finally, the system was constructed so that a layer of lead--approximately 0.375 in. thick in any radial direction from the target--could be inserted between the target and the scintillation counters. The purpose of the lead was to convert γ rays from the neutral pions resulting from antiproton annihilation.

A photograph of the complete counter assembly as seen during the experiment is shown in Fig. 8.

D. Electronics and Antiproton Identification

A simplified block diagram of the basic electronics is shown in Fig. 9. The electronic identification of antiprotons was accomplished first by a fast coincidence (resolution of $\approx 4\times10^{-9}$ sec) of the scintillation counters S_1, S_2, and S_3 in anticoincidence with the meson counter $\overline{C}$. Another coincidence circuit received the signals from the three VSC II photomultipliers to produce the final VSC II signal. Finally a third coincidence circuit placed VSC II in coincidence with $S_1S_2S_3\overline{C}$ and thus signaled the transmission of an antiproton through the magnetic channel and its incidence on the hydrogen target. As seen in Table II, this system had a pion-rejection rate of 3×10^{-6}%; thus the ratio of pions counted accidentally to the total number of pions that pass through the system was 3×10^{-8}. Since the ratio of pions to antiprotons is approximately 5×10^{4}, there was only one accidental pion in every 10^{3} electronically identified antiprotons. However, even further discrimination against this small background was made by the photographic method described below.

As schematized in Fig. 9, the identified antiproton (i.e., the output of the 2×10^{-8} coincidence) was put in coincidence with each of the counters surrounding the hydrogen target by means of the 27 two-channel coincidence circuits. Each of the 27 possible outputs was delayed sequentially with alternate polarities for oscilloscope presentation and each output was gated to eliminate mutual interference. The identified $\overline{p}$ signal was also used to trigger a four-beam oscilloscope, which displayed the 27 two-channel coincidence outputs along with the beam counters used to produce the trigger. The drawing in Fig. 10a shows the positions of all possible pulses. Traces 1 and 2 display the beam counters with the exception of VSC II. Here the final discrimination against the remaining pion contamination was made by rejection of any event that had a $\overline{C}$ pulse. This was approximately one event in a thousand. Since S_2 and $\overline{C}$ had the same polarity, they were electronically gated so that an accidental S_2 pulse could not simulate $\overline{C}$, and vice versa.

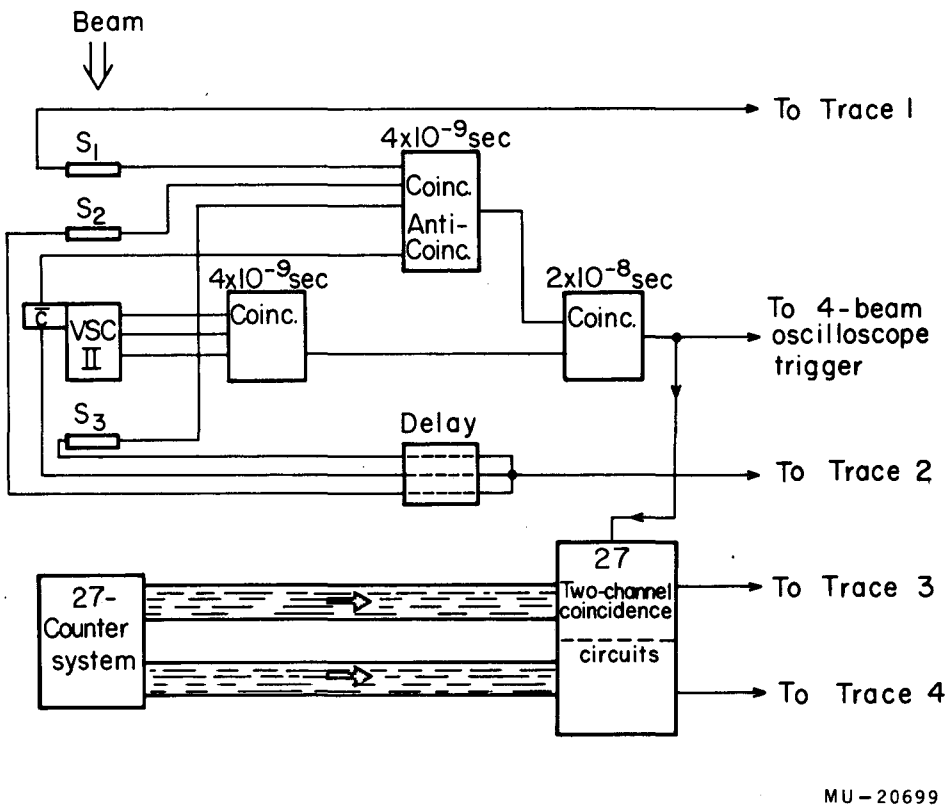

Fig. 9. Simplified block diagram of the basic electronics.

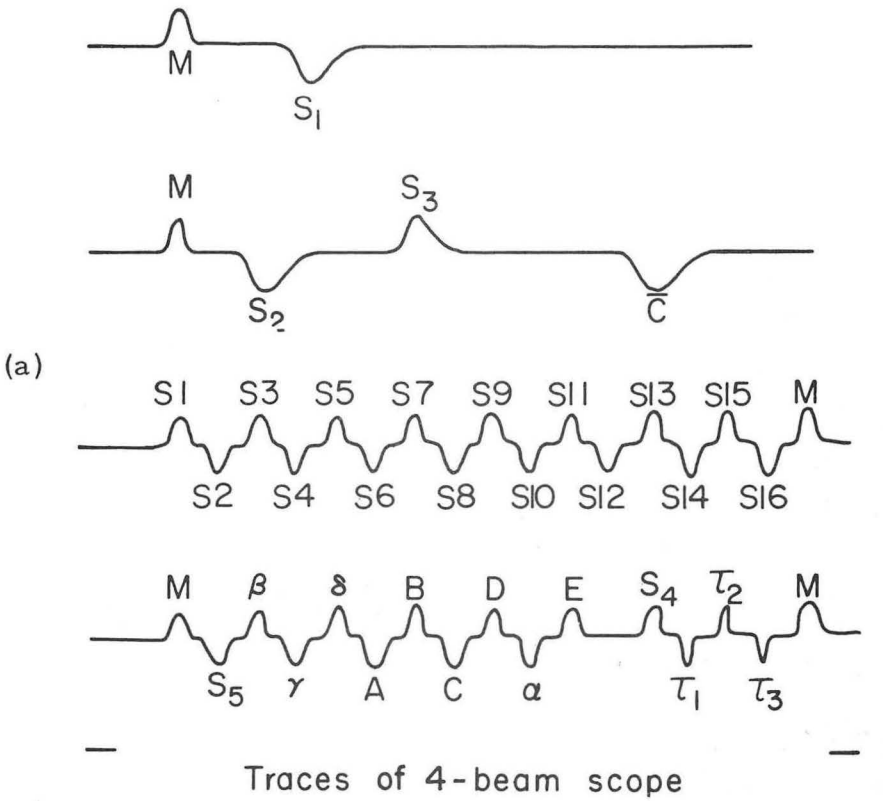

(b)

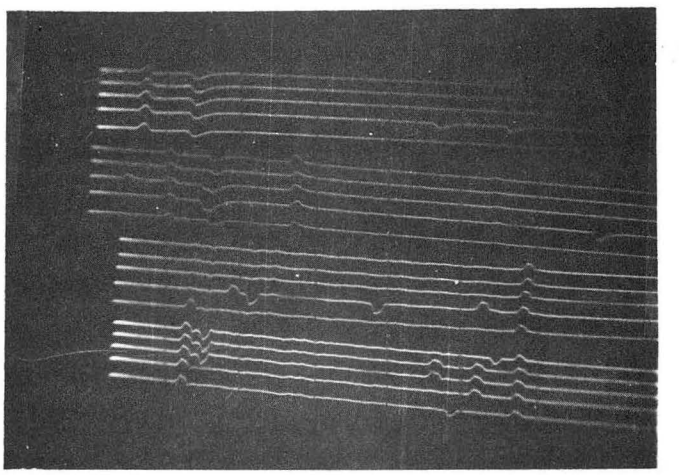

ZN-2555

Fig. 10. (a) Positions of all possible pulses on oscilloscope film.

(b) Actual photo of five events. All five events are seen to have pulses S_1, S_2, S_3 and not $\overline{C}$, thus identifying five incident antiprotons. In the first three events only counters S_4 or S_5 or both signal, which means the antiproton did not interact. In the fourth event the antiproton annihilated, sending pions into counters S3, S4, S10, and S15. In the last event only a single count is detected in S1, which is typical of an elastic scattering into that counter.

In addition, the time-of-flight criterion was made more stringent by the measurement of the relative positions of S_1, S_2, S_3 to within 2 nanoseconds. The pulses labeled M are timing markers used for identification of the positions of the other pulses; $\tau_1 \tau_2$, and τ_3 are beam-spill-time indicators used to identify more accurately the Bevatron energy at which the antiproton was formed.

The oscilloscope traces were photographed on 35 mm film. As many as six events could be recorded during a Bevatron pulse without interference between the various traces. Figure 10b is an actual photograph of the film in which five events are seen. The top trace of each of the four groupings is the first event.

III. PROCEDURE

A. Data Accumulation

The experimental run can be divided into four sections in which major experimental conditions for the study of the interaction cross sections were varied. These sections were chronologically

(1) Hydrogen target--lead converter in.

(2) Deuterium target--lead converter in.

(3) Deuterium target--lead converter out.

(4) Hydrogen target--lead converter out.

During each condition above, the five selected momenta were run in sequence and, for each momentum, runs were made alternately with hydrogen (or deuterium) target full and then empty. To obtain statistical accuracy, especially in view of the $\bar{p}$-d - $\bar{p}$-p subtraction, it was necessary to have nearly 10,000 antiprotons incident at each momentum for each of the four conditions; thus approximately 200,000 $\bar{p}$ events were recorded in the entire experiment.

Additional changes in Bevatron internal targets were made during some of the above runs in order to study antiproton production. These changes affected only the flux of antiprotons through the magnetic channel. A special run was made for the $\bar{p}$ excitation function in which the Bevatron energy was varied.

Information on $\bar{p}$ production and on the $\bar{p}$-p (or $\bar{p}$-d) total cross sections was electronically monitored on scalers during the course of the experiment. The electronic information was found to be in agreement with the film data in all cases. In order to obtain the antiproton partial-interaction cross sections the oscilloscope film had to be analyzed. The film was scanned visually and the information recorded on special data sheets for rapid tabulation.

B. Classification of Antiproton Interaction Events

The particular geometry of the counter system surrounding the hydrogen target was influenced to some extent by prior information on the $\bar{p}$-p interaction at low energies. To be more specific, the antiprotons that enter the hydrogen target can interact principally in three ways. They can

(a) scatter elastically,

(b) annihilate or inelastically produce mesons,

(c) charge-exchange.

From the low-energy data[17, 18, 19] we know that the elastic scattering is peaked in the forward direction and that, upon annihilation, 4.8π mesons (about 2/3 of them charged) are produced on the average.

In view of these factors, half the interaction detection counters (see Figs. 6 and 7) were designed to cylindrically surround the target, for the purpose of detecting the major fraction of the annihilation pions. The remaining counters formed concentric rings in the forward direction. Their principal task was to detect elastically scattered antiprotons as well as some of the annihilation pions. The central disc counters S_4 and S_5 detected the noninteracting antiprotons.

As mentioned in Section II-D, whenever an identified antiproton (i.e., electronically certified by the $S_1S_2S_3$ VSC II $\bar{C}$ trigger) entered the hydrogen, all the counters surrounding the hydrogen were interrogated. The resulting information was photographed on the oscilloscope and classified as follows:

(a) Pass-Throughs. If the good-geometry counters S_4 or S_5 or both were the only counters that signaled, the antiproton passed through the hydrogen without interaction.

(b) Elastic Scattering. If a single counter of the small-angle rings counted, it was considered an elastic scattering event, since the recoil proton did not have sufficient energy to leave the target. However, in the larger rings it was possible to have an additional counter signal due to the recoil proton. This latter event was accepted as an elastic scattering only if the event was coplanar within the finite counter size.

(c) Inelastic Scattering or Annihilation. This was the classification for events in which any three or more counters signaled. It also includes those two-counter events in which the kinematics were not consistent with elastic scattering.

We note that annihilation events of the type $\bar{p} + p \rightarrow \pi^+ + \pi^- + n\pi^0$ (where n is an integer of average value ≈ 3) are not confused with elastic scattering chiefly because of the coplanarity condition. This was verified when the lead converter was used and the number of elastic scattering events remained unchanged. The particular annihilation mode, $\bar{p} + p \rightarrow \pi^+ + \pi^-$, of course cannot be distinguished from elastic scattering. However, this mode was not observed in bubble chamber experiments at low energies,[18, 19] and thus can be estimated to constitute less than 0.3% of all annihilations. The other possible annihilation modes are unambiguous.

(d) Charge Exchange. This final classification is for the events in which none of the surrounding counters gave a signal and therefore a charge-exchange event of the type $\bar{p} + p \rightarrow \bar{n} + n$ was assumed to take place. This classification can be simulated by annihilations that produce only π^0 mesons; however, runs with and without lead converter showed that any correction was within the statistical error of the charge-exchange cross section. This again agrees with previous estimates.[18, 19]

C. Experimental Checks

1. Proton-Proton Cross Sections

Although we felt that the antiproton events could be positively identified by the system described in the preceding sections, conclusive tests were made. One method of testing the entire system is to measure well-known cross sections such as proton-proton cross sections. To do this, positive proton beams were formed by scattering a 1.2-Bev internal Bevatron beam from an additional target in the position denoted by T in Fig. 1. With all magnet currents reversed, the positive protons traversed the magnetic channel and entered the hydrogen target in precisely the same way as the antiprotons. The proton-proton cross sections were measured at two energies and the results are presented in Table III. Excellent agreement was obtained with the results of other experiments.[20, 21]

Table III

p^+-p cross sections for two energies

p^+ energy (Mev)	p^+-p cross sections (mb)		
	Total	Elastic	Inelastic
528	30 ± 7	24 ± 5	6 ± 3
940	49 ± 5	26 ± 3	23 ± 3

2. Tests for Accidental Coincidences

The 27 counters surrounding the hydrogen target were subject to accidental counts resulting from the high flux of neutrons in the Bevatron experimental area. The concrete shielding around the area A (Fig. 1) was not sufficient to eliminate this background entirely. To determine the accidental rate a number of runs were made during which the $\overline{p}$ trigger from the 2×10^{-8}-sec coincidence (Fig. 9) was put out of delay with respect to each of the 27 signals from the counters encircling the hydrogen target. The oscilloscope traces were photographed as in a normal run. Any pulses that occurred during this time were due to the accidental counts. The results showed that an average counter had a probability of $\approx 1.5\times10^{-3}$ for counting accidentally during a real event. Corrections were made for this effect in the final analysis.

IV. ANTIPROTON PRODUCTION

A. Production in Hydrogen

The measurement of antiproton-production cross sections is still a difficult task. This is because no external proton beams of sufficient energy and intensity exist at present. Consequently one has to perform such experiments by utilizing the internal circulating beam of the Bevatron. It seemed possible that antiproton production in p-p collisions might be measured (by CH_2-C subtraction) at the same time as the antiproton-interaction cross sections were being measured. The high production rate for hydrogen indicated by a previous experiment[12] served as an incentive to explore the production phenomenon more accurately in this experiment. Target-flipping mechanisms were developed which could flip either the C or the CH_2 targets to identical positions within the Bevatron. The C and CH_2 targets themselves were designed to have the same number of carbon atoms and at the same time possess identical physical dimensions. This was accomplished by cutting holes in the carbon target. Extensive measures were also undertaken--through the installation of a primary lip and various clipping devices around the Bevatron tank--to insure negligible probability that the internal-beam protons would hit the target holders and to insure that they would be stopped after one traversal of the target. To dispose of possible unknown systematic errors in the Bevatron beam, the C and CH_2 were used alternately on each Bevatron pulse.

The results of this experiment contradict the previous results[11, 12] in that antiproton production in hydrogen was found negligible compared to production in carbon. The ratio of the differential cross section for production (for 1684-Mev/c antiprotons produced at 0 deg by 6.0-Bev protons) by a free proton to production by a carbon nucleus was found to be -0.035 ± 0.025. This is to be compared with the value $+0.11 \pm 0.06$, obtained from the earlier estimates.[11, 12]

The only conclusions that can be reached now are that production in hydrogen is very small and that more accurate measurements must await an external proton beam which can be used in conjunction with a liquid hydrogen target and thus avoid the subtraction process.

B. Production in Carbon

After failing to observe antiproton production in hydrogen, we used carbon targets exclusively during the remainder of the experiment and considerable data were accumulated on antiproton production in carbon. Information on the excitation function, momentum distribution, and angular distribution respectively is presented in the following paragraphs.

Excitation Function

The only prior information on the production of antiprotons as a function of Bevatron energy consisted of three experimental points for 1200-Mev/c antiprotons produced in a copper target.[1] This information was not sufficient for determining the shape of the excitation function. In Fig. 11 we present the results of this experiment for the production of 1684-Mev/c antiprotons. The experimental points were determined by counting the antiprotons traversing our magnetic channel and monitoring the Bevatron internal beam incident on our carbon target by means of the Bevatron induction electrodes.[22] Corrections were made for detection efficiency, transmission through the magnet system, and absorption by material in the beam; therefore, the experimental points actually refer to production at the Bevatron target. No correction has been made for self-absorption in the carbon target.

In order to analyze antiproton production within a nucleus, one must make an assumption as to the basic interaction process. Here we first assume that antiprotons are produced in carbon by the proton-nucleon processes

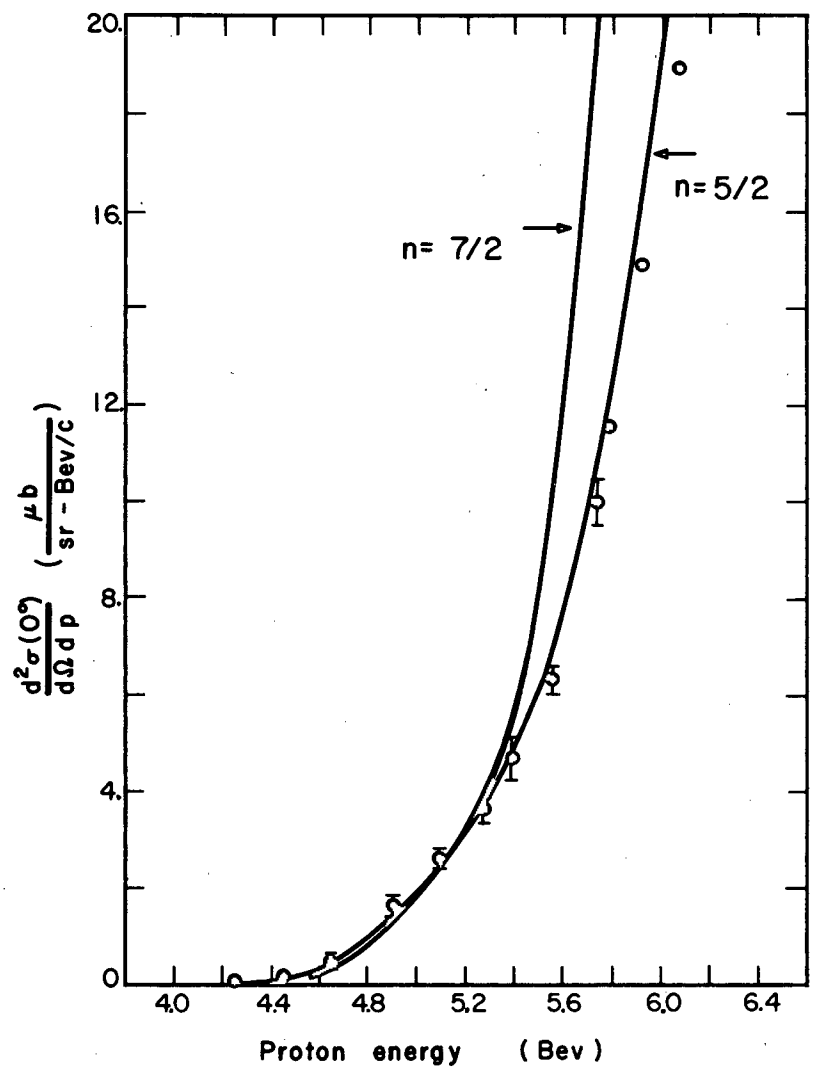

MU-20701

Fig. 11. Excitation function for 1684-Mev/c antiprotons produced at 0 deg in carbon. The experimental points correspond to the number of antiprotons produced externally to a 2-in.-long carbon target. The curves are taken from a statistical model.

$$p + n \rightarrow \bar{p} + p + p + n \,, \tag{4}$$

$$p + p \rightarrow \bar{p} + p + p + p \,. \tag{5}$$

(Other possible processes, such as the production of antiprotons by pion-nucleon collisions, are mentioned briefly at the end of this section.) High-energy processes with multiparticle final states are most easily analyzed by statistical methods, owing to the difficulty involved in more precise theoretical calculations. For the particular reactions above, (4) and (5), statistical calculations have been made by Amaldi et al.[23] in order to predict the relative yield of antiprotons in the laboratory system as a function of antiproton momentum and angle of emission. These calculations assume that the production cross section is proportional only to the volume of phase space available, and that the kinetic energy available in the center-of-mass system is distributed among the four final-state particles according to statistical factors. The nucleons in the nucleus are considered to be a completely degenerate Fermi gas with maximum energy of 25 Mev; this nucleon distribution is folded into the calculations. Thus Amaldi et al. arrived at a formula for the distribution of antiprotons as a function of their momentum and angle and also of the incident proton energy:

$$S_n(p, \mu)dp\, d\mu = \frac{105}{16} \frac{p^2}{\sqrt{p^2+1}}\, dp\, d\mu \int_{4.0}^{W_{0\,max}} \frac{P(W_0)\,(W_0-4)^n \left\{1-\left(\frac{p^*}{p^*_{max}}\right)^2\right\}^2 \sqrt{(p^*)^2+1}\, dW_0}{(p^*_{max})^3} \tag{6}$$

where

W_0 = the total energy in the center-of-mass system (in units of m_p),

$(W_0-4)^n$ = phase-space volume where $n = 7/2$ for Eq. (4) and $n = 9/2$ for Eq. (5),

p^* = antiproton center-of-mass momentum,

p = antiproton laboratory-system momentum,

$\mu = \cos\theta$, where θ is the laboratory-system angle of emission with respect to the forward direction,

$P(W_0)dW_0$ = the probability that W_0 (in the center-of-mass system) of the incident nucleon and one nucleon in carbon lies between W_0 and $W_0 + dW_0$.

It is given by the expression

$$P(W_0) = \frac{3W_0}{2B}\left\{1 - \left[\frac{B}{2A} - \left(\left(\frac{B}{2A}\right)^2 + \frac{W_0^{\,2} - C}{A}\right)^{1/2}\right]^2\right\},$$

where

$$A = 2\,T_f\,(T + 1)\,,$$
$$B = \left[8\,T_f\,(T^2 + 2T)\right]^{1/2}\,,$$
$$C = 2\,(T + 2)\,,$$

and T is the incident proton energy (lab) and T_f is the maximum Fermi energy expressed in proton mass units (m_p). $P(W_0)$ may be found plotted explicitly for $T = 6.5$ in Fig. 7 of Ref. 23. We have used Eq. (6) and evaluated S_n ($p = 1684$ Mev/c, $\mu = 1$) as a function of incident proton energy for the two cases $n = 5/2$ and $n = 7/2$. The results are plotted in Fig. 11 along with the experimental data. A rather arbitrary normalization of the calculated results has been made with the experimental point at 5.1 Bev.

In Fig. 11 one sees that the threshold for antiproton production in carbon is about 4.3 Bev. This would be expected from Processes (4) and (5) when the target nucleons have a maximum Fermi energy of 25 Mev, the value assumed in the statistical calculations. This feature lends support to the initial assumption that proton-nucleon collisions are primarily responsible, as much lower thresholds would be noticed for reactions such as (7) and (8) below.

There are of course other factors (which we will only mention) that could modify the calculated excitation curves of Fig. 11. One could explore other nuclear models to modify the function $P(W_0)$. There

is also the possibility that other processes, aside from (4) and (5)--such as the formation of deuteron or helium nuclei in the final state--could modify the curves. Lastly, the assumptions of a statistical model are always subject to some question.

Production of antiprotons can possibly also take place by a two-step reaction within the carbon target if a high-energy pion is first made by a proton-nucleon collision. The pion then proceeds to initiate one of the following reactions:

$$\pi^- + p \rightarrow \bar{p} + p + n \,, \tag{7}$$

$$\pi^+ + n \rightarrow \bar{p} + p + p \,. \tag{8}$$

The threshold at the Bevatron to produce a pion of sufficient energy in carbon (again assuming 25 Mev for the maximum Fermi energy) is about 3.2 Bev. Although no antiprotons were detected at our lowest energy of 4.25 Bev (see Fig. 11), we cannot rule out (7) and (8), as the pion flux in the carbon target is considerably smaller than the proton flux. We can only estimate that the cross section for production of antiprotons by pions is probably no greater than for the production by protons.

Momentum Distribution

Data on the production of antiprotons as a function of their momenta are given in Table IV. Information from other experiments[8,17,24] is also presented for comparison. Although the other experiments used a beryllium target instead of a carbon target, the difference should be negligible for the type of high-energy process under consideration. In the next section we find that differences in angles of emission such as those seen in Table IV have little effect on the comparison between various momenta. The fifth column of the table gives the ratio of pions transmitted down the magnetic channel to incident protons on the target. This ratio is presented to show that the number of pions versus momentum is relatively constant in any given experimental arrangement and that one is therefore able to use the pions to monitor the $\bar{p}$ rates.

Thus column 6 ($\bar{p}/\pi^-$) should, to a fair approximation, represent the relative antiproton production rate. The data are plotted in Fig. 12.

For column 7 of Table IV we have calculated the more desirable ratio of antiprotons to incident protons for this experiment. These numbers have been corrected for counting efficiency and losses along the magnetic channel, so that they actually refer to antiprotons produced at the carbon target. Although the relative values of $\bar{p}/p^+$ are probably accurate, there is about a 20% uncertainty in the absolute p^+ monitor. Because of this factor and differences in the targets as well as solid angles of acceptance and transmissions of the various spectrographs, this ratio is not tabulated for the other experiments listed in the table. Discrepancies of this nature are probably reflected by the variations seen in column 5.

In Fig. 12 experimental data are again compared with a statistical model.[23] The curve shown is obtained from (6) for $n = 7/2$, $T_{p^+} = 6.1$ Bev, $\theta = 0$ deg, and it is normalized to the experimental point at 1684 Mev/c. It is seen that the model has reasonably indicated the shape of the momentum distribution. To relate the ordinate of Fig. 12 to cross section for the data of this experiment, the 1684-Mev/c point should be compared to the 14.9-μbarn/sr(Bev/c) point in Fig. 11. In making such a normalization one should actually use the column $\bar{p}/p^+$ in Table IV for correctness; however, if the column $\bar{p}/\pi^-$ (plotted in Fig. 12) is used, the result is not appreciably different in the momentum range of this experiment.

Table IV

Production of antiprotons of various momenta by 6-Bev protons

Momentum (Mev/c)	Angle of emission (deg)(lab)	Target length (cm)	Target material	π^-/p^+ [a] (10^{-7})	$\bar{p}/\pi^-$ [a] (10^{-5})	$\bar{p}/p^+$ [b] (10^{-11})	Reference
1200	5	5.08	carbon	12	1.80±0.03	13.8±0.2	This experiment
1400	3	5.08	carbon	11.2	2.86±0.03	22.1±0.3	This experiment
1531	1.5	5.08	carbon	11.8	3.55±0.04	34.7±0.4	This experiment
1684	0	5.08	carbon	11.8	3.80±0.04	39.2±0.4	This experiment
1825	1.5	5.08	carbon	11.9	3.62±0.03	37.4±0.4	This experiment
1700	0	15.3	beryllium	13.0	4.5 ±0.5		Ref. 24
2000	0	15.3	beryllium	12.0	4.8 ±0.5		Ref. 24
2800	0	15.3	beryllium	9.0	2.9 ±0.9		Ref. 24
750	8.5	15.3	beryllium	8.0	0.2 ±0.12		Ref. 8
900	3	15.3	beryllium	12.0	0.4 ±0.24		Ref. 8
1150	2.5	15.3	beryllium	20.0	1.2 ±0.7		Ref. 8
1410	6.2	15.3	beryllium	22.0	1.9 ±1.1		Ref. 8
600	0	15.3	beryllium	40.	0.15±0.07		Ref. 17
700	0	15.3	beryllium	50.	0.24±0.12		Ref. 17
800	0	15.3	beryllium	50.	0.44±0.22		Ref. 17
900	7	15.3	beryllium	60.	0.80±0.40		Ref. 17

[a] Transmitted through magnetic channel

[b] Corrected at carbon target

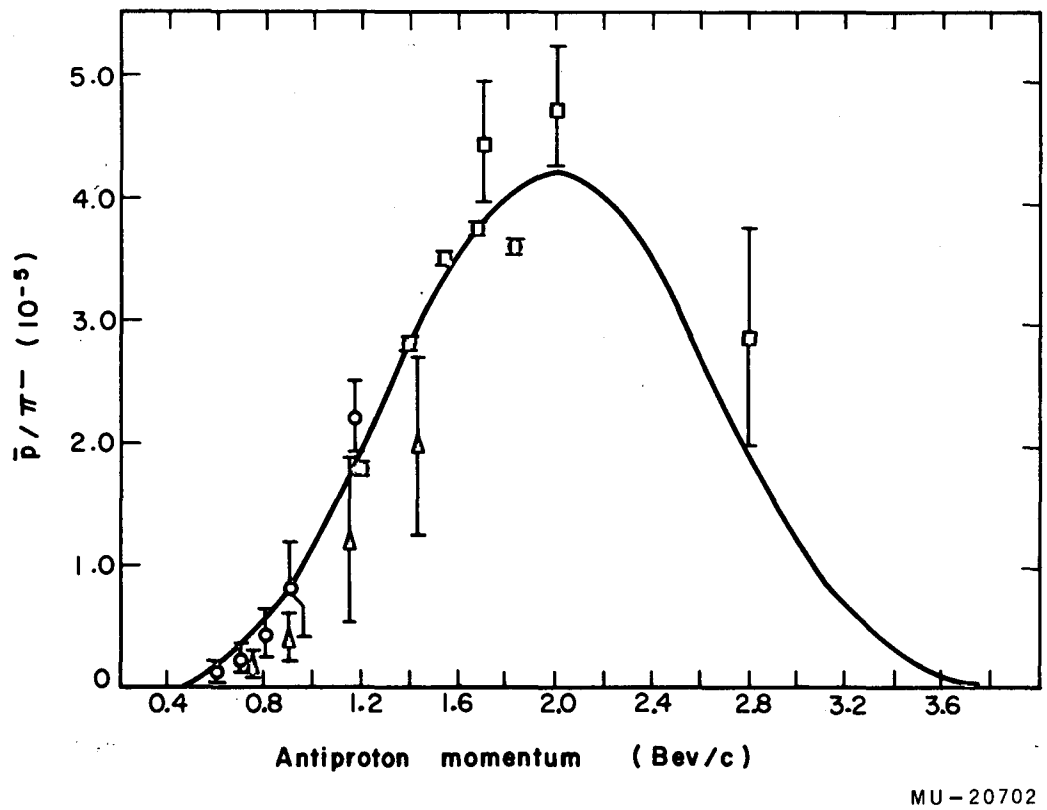

Fig. 12. Momentum distribution for antiprotons produced by approx 6-Bev protons on carbon and beryllium. The experimental points are taken from Table IV. The curve is calculated by a statistical model (Eq. (6)).

Angular Distribution

Results on the angular distribution were obtained for three momenta. As only three targets were available within the Bevatron, three angles of emission were observed for each momentum. In Table V one sees that the production rates do not change appreciably within the angular intervals used in this experiment. For 6.1-Bev protons, the statistical model--i.e., (6)--predicts that the relative antiproton production rate should fall (relative to 1.0 at 0 deg) to 0.8 at 8 deg, and to 0.5 at 15 deg, and approach zero at 25 deg. Owing the small differences in the angles of emission for this experiment, no significant comparison can be made.

Table V

Antiproton production rates versus angle of emission in the forward direction

Antiproton momentum (Mev/c)	Angle of Emission (deg) (lab)	$\bar{p}/p^+$ (10^{-11})
1400	3	22.1±0.3
1400	13	20.3±1.4
1400	7	22.2±0.7
1531	1.5	34.7±0.4
1531	11	34.2±1.2
1531	8	35.2±0.9
1684	0	39.2±0.4
1684	9	37.0±0.8
1684	8.5	36.1±0.9

V. ANTIPROTON-PROTON CROSS SECTIONS

A. Calculations and Results

The antiproton-proton interaction events, identified by the methods described earlier and classified according to the four categories enumerated in Section III-B, were used to calculate the fundamental $\bar{p}$-p cross sections by means of the following formulas:

$$\sigma_t = \frac{1}{N} \ln \left(\frac{I_0}{I} \times \frac{I'}{I_0'} \right), \tag{9}$$

$$\sigma_i = \frac{1}{N} \ln \left(\frac{I_0}{I_0 - I_i} \times \frac{I_0' - I_i'}{I_0'} \right), \tag{10}$$

$$\sigma_e = \frac{1}{N} \ln \left(\frac{I + I_e}{I} \times \frac{I'}{I' + I_e'} \right), \tag{11}$$

$$\sigma_c = \frac{1}{N} \ln \left(\frac{I + I_e + I_c}{I + I_e} \times \frac{I' + I_e'}{I' + I_e' + I_c'} \right), \tag{12}$$

where

I_0 = the number of incident antiprotons,
I = the number of pass-throughs,
I_i = the number of inelastic events,
I_e = the number of elastic scatters,
I_c = the number of charge exchanges,
N = the number of protons/cm^2 in the target.

The unprimed quantities in the foregoing equations refer to measurements made with the hydrogen target full, while the primed quantities refer to background measurements obtained when the target container was empty. Formulas (9) through (12) are derived in the Appendix.

Experimentally one imposes the restrictions

$$I_0 = I + I_i + I_e + I_c , \tag{13}$$

$$I_0' = I' + I_i' + I_e' + I_c' . \tag{14}$$

from these relations it is easily seen that the cross-section formulas above can be combined to yield the anticipated result,

$$\sigma_t = \sigma_i + \sigma_e + \sigma_c \, . \tag{15}$$

The analysis of all the antiproton-proton interaction events has yielded the results given in Table VI for the five antiproton energies investigated here.

Table VI

$\bar{p}$-p cross sections at various energies

$\bar{p}$ energy (Mev)	Cross sections (mb)			
	Total	Elastic	Inelastic	Charge-exchange
534±25	118±6	42±5	70±3	6.0±1.3
700±33	116±5	42±4	66±3	7.2±1.5
816±37	108±5	38±4	63±3	7.1±1.2
948±42	96±3	33±3	56±2	6.8±1.0
1068±46	96±3	30±2	60±2	5.7±1.1

B. Corrections and Uncertainties

The errors quoted in Table VI are chiefly the standard deviations due to counting statistics together with some uncertainty in the following corrections which were made.

The Total Cross Section

The total cross sections were corrected for forward scattering. This was done by measuring the cross sections at three different cutoff angles (3, 4.2, and 5.3 deg) determined by counters S_4 and S_5. These results were plotted versus solid angle (determined by the cutoff angle) and extrapolated to zero solid angle by a straight-line least-squares fit. The result gave the same correction factor as one would obtain by use of the optical theorem[25] and the assumption $d\sigma/d\Omega(0^\circ) \approx I_0^{\,2}$, where I_0 is the imaginary part of the forward-scattering amplitude. This correction factor (3 deg to 0 deg) amounted to approximately 2 mb.

Small corrections of the order of 1% to 2% have been made for accidentals (see Section III.C) and for annihilations in counters S_4 and S_5.

Elastic-Scattering Cross Section

The same correction for forward scattering has been made as in the total cross section, as well as similar corrections for accidentals and annihilations in counters and surrounding material. An additional correction (≈1%) has been made for scatterings that find their way through small cracks between counters and thus simulate charge exchange.

No correction has been made for backward-scattered antiprotons, that may not have sufficient energy to leave the target and hence annihilate in the hydrogen, because of the uncertainty in the angular distribution at large angles. It is noted, however, that experiments at lower energies (100 to 480 Mev),[17, 18, 33] where the angular distributions are known to large angles, indicate that this correction would probably be negligible.

Inelastic Cross Section

Here the sum of the two previous corrections to the total and the elastic cross sections for annihilations in counters and for accidentals has been subtracted.

Charge-Exchange Cross Section

For the charge-exchange cross sections corrections have likewise been made for antineutron annihilations in the surrounding counters, for accidental events that would make a charge exchange appear as a pass-through or elastic scattering, and for the small fraction of one-count elastic scatterings that travel through a crack between counters, thus recording spuriously as charge-exchange events.

A correction that has also been considered is for the effect due to annihilations entirely into π^0 mesons. During the runs with and without lead converter for the π^0 gamma rays, no appreciable change was detected in the charge-exchange cross section; however, estimates from bubble chamber data[18,19] indicate that possibly 20% of the charge-exchange cross section determined without converter could be due to zero-prong annihilations. If this were true, one would subtract $\approx$1.5 mb from σ_c and add it to σ_i. Theoretical results at $\approx$ 140 Mev[26] are in agreement with this estimate. We have accordingly corrected the portion of the data obtained without lead converter to give the final results presented in Table VI.

C. Discussion of Results

1. General Features

The results for the antiproton-proton cross sections given in Table VI are plotted in Fig. 13 for the purpose of comparing them with the cross sections obtained by others at lower $\bar{p}$ energies[7, 8, 17, 18, 19, 27] and in a recent experiment[28] at higher energies. One sees a reasonable transition between the low-energy cross sections, and those determined by this experiment. There is excellent agreement between our highest-energy points and the data of Ref. 28. From 500 to 1000 Mev the $\bar{p}$-p cross sections still remain much larger than nucleon-nucleon cross sections in this energy range.

The general trend of the $\bar{p}$-p cross sections is a slow decrease with increasing energy; the cross sections vary approximately as $1/T_{\bar{p}}^{-1/2}$ where $T_{\bar{p}}$ is the antiproton laboratory-system kinetic energy. Although the charge-exchange cross section appears to be nearly a constant 7 mb in our energy range, it is not inconsistent with the energy dependence of the other cross sections. Our values for the charge-exchange cross section are in agreement with other values obtained by different methods and near the energies under discussion here. For example, Weingart et al.[29] obtained the value 10.9±5.8 mb at 455 Mev. They used a C and a CH_2 target to initiate the charge exchange and a large block of plastic scintillator to detect the antineutron annihilation. A recent experiment in the 72-in. hydrogen bubble chamber, using 930-Mev antiprotons,[30] has yielded a value of 8.5±0.9 mb for the charge-exchange cross section.

At this point, the clarification of a puzzling situation created by two prior experiments[7, 8] should be mentioned, as there has been considerable speculation on whether the prior data were in serious error.[9] The problem can be clearly seen if one observes Table VII.

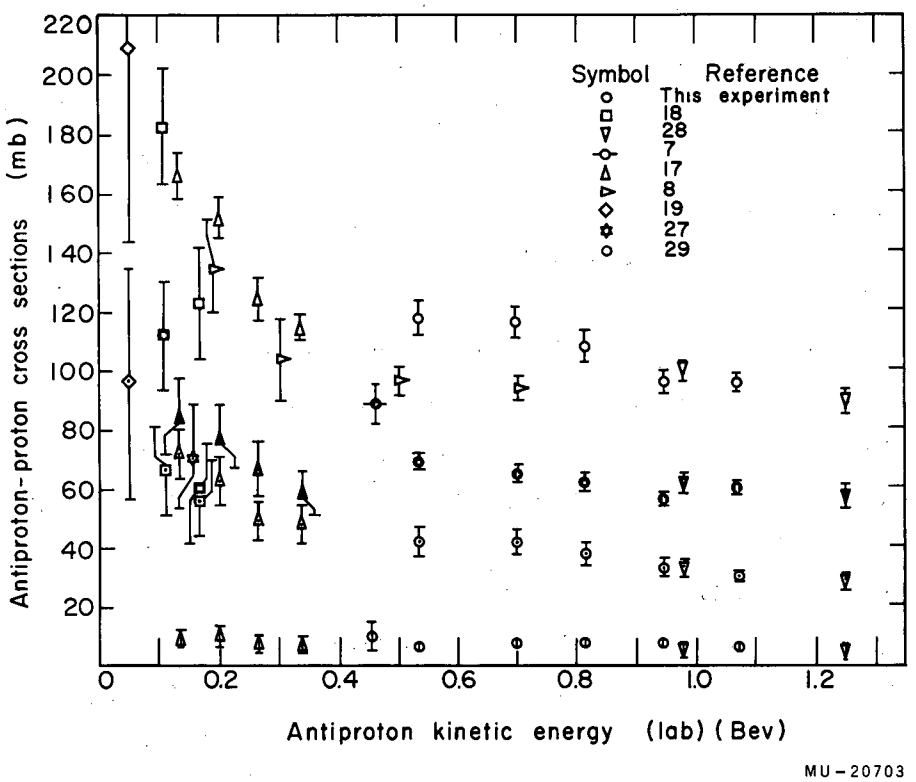

Fig. 13. $\bar{p}$-p cross sections as a function of antiproton kinetic energy. The open symbols are total cross sections; closed symbols are inelastic cross sections (for $T_{\bar{p}} < 288$ Mev they are annihilation cross sections); open symbols encircling a dot are elastic cross section; open symbols crossed by a vertical line at the bottom of the figure are charge-exchange cross sections. The various types of symbols refer to different experiments; the references are correlated with the symbols in the upper right corner of the figure.

Table VII

Comparison of $\bar{p}$-p cross sections near 500 Mev

Experiment	Total (0 deg)	Total (14 deg)	Inelastic	Elastic	Charge-exchange
Chamberlain et al.[7] (457 Mev)	--	104±8	89±7	--	--
Cork et al.[8] (500 Mev)	97±4	--	--	--	--
This experiment (534 Mev)	118±6	93±5	70±3	42±5	6±2

If the cross sections of Refs. 7 and 8 are taken at their face value, there is -7±11 mb of diffraction scattering between 0 and 14 deg (lab), with an absorption cross section very nearly equal to the total cross section. Using the results of this experiment the difficulties can be removed by the following conclusions:

(a) The 89 mb of Chamberlain et al.[7] is perhaps 20 mb high.

(b) The 97 mb of Cork et al.[8] is 20 mb low.

(c) The σ_t(14 deg) of Chamberlain et al. is reasonable.

Owing to the circumstances that (a) and (b) correct possible errors in opposite directions, one was forced to conclude that there was a large absorption cross section without diffraction scattering. The results of this experiment should be more reliable, as a more effective means of detecting the annihilation process was used and the elastic as well as the total and annihilation cross sections could be measured simultaneously. For example, the cross sections of Cork et al.[8] are consistently lower than their later values,[17] obtained by methods similar to those of this experiment. The inelastic cross section of Chamberlain et al.[7] was subject to a larger statistical uncertainty than this experiment because of the H_2O-O_2 subtraction procedure. There was some additional uncertainty in their method of detecting the annihilation events. Our present results show that the diffraction scattering near 500 Mev is approximately 1/3 of the total cross section, and is sharply peaked in the forward direction.

2. The Ineastic Process

It is of interest to consider the behavior of the inelastic cross section near 300 Mev. The inelastic cross section as defined earlier is due entirely to the annihilation process below 288 Mev, while above this energy the following processes may also be included:

$$\bar{p} + p \rightarrow \bar{p} + p + \pi^0 \tag{16}$$

$$\bar{p} + p \rightarrow n + \bar{p} + \pi^+ \tag{17}$$

$$\bar{p} + p \rightarrow \bar{n} + p + \pi^- \tag{18}$$

In Fig. 13 an apparent rise in the inelastic cross section can be noticed between 350 and 500 Mev, if one considers the data of this experiment together with those of Coombes et al.[17] This effect is possibly due to the onset of pion-production processes such as the ones listed above. These processes have the distinctive feature that only two charged particles are produced in the final state; thus the analysis of our two-particle inelastic events obtained with lead converter allows us to estimate the cross section for (17) and (18). The same procedure cannot be done for (16) without the use of the lead converter, because of its being indistinguishable from the more abundant annihilation mode (19):

$$\bar{p} + p \rightarrow \pi^+ + \pi^- + n\pi^0 . \tag{19}$$

The results indicate that the inelastic processes (17) and (18) comprise together approx 5 mb of the inelastic cross section at each of the anti-proton energies of this experiment. This value of 5 mb is about half the value for the similar processes

$$n + p \rightarrow p + p + \pi^- , \tag{20}$$

$$n + p \rightarrow n + n + \pi^+ , \tag{21}$$

observed at 980 Mev.[21] This may be due to the strong competition with the annihilation process in the $\bar{p}$-p case. Goldhaber et al.[33] have observed a few events of the type (16) through (18) in an experiment in which 480-Mev antiprotons interacted in the 30-in. propane bubble chamber. As the events of this type are difficult to identify if the anti-proton leaves the chamber, they do not yet have an estimate of the cross section.

In the n-p interaction at 980 Mev[21] the process

$$n + p \rightarrow n + p + \pi^0 \tag{22}$$

has twice the cross section of Processess (20) and (21) combined. If this ratio should persist for $\bar{p}$-p interaction, one could say that meson production by $\bar{p}$-p collisions could be as high as 15 mb. Consequently, from our value of σ_i (in Table VI) at 948 Mev, the annihilation cross

section would have 41 mb as a lower limit. This estimate, in view of the manner by which it was attained, rests on the assumption that double-pion production is negligible, as it is in the p-p and n-p interactions below 1 Bev.[21, 31, 32]

We will not attempt to present an analysis of annihilation events according to their pion multiplicity, because of the poor resolution of our counter system for high multiplicities. For multiplicities greater than 4, there is a strong probability that two pions will enter the same counter. Further corrections arise from the pion-production processes mentioned in the last paragraph, the annihilations into strange particles, pion interactions within the hydrogen target after annihilation, and the escape of some pions through cracks between counters.

3. Angular Distribution of Elastic Scattering

The experimental points for the angular distribution of antiproton-proton elastic scattering are plotted in Figs. 14, 15, and 16 for the various antiproton energies. From the figures it is seen that most of the elastic scattering is peaked forward with 40 deg (center-of-mass angle). Although our system could detect elastic scattering from 40 to about 135 deg, the angle of scattering could not be determined within this interval. For the energy interval of this experiment only a few millibarns of the total elastic scattering cross section are attributed to scatters greater than 40 deg. The experimental point at 0 deg is a lower limit determined by means of the optical theorem from the total cross section measurements. (See Section V. B.)

In Fig. 16 we have plotted for comparison the data of a recent experiment[24, 28] near the same energy. Armenteros et al. performed their experiment with techniques similar to this experiment, but had better angular resolution, especially at large angles. The two sets of data are in very good agreement.

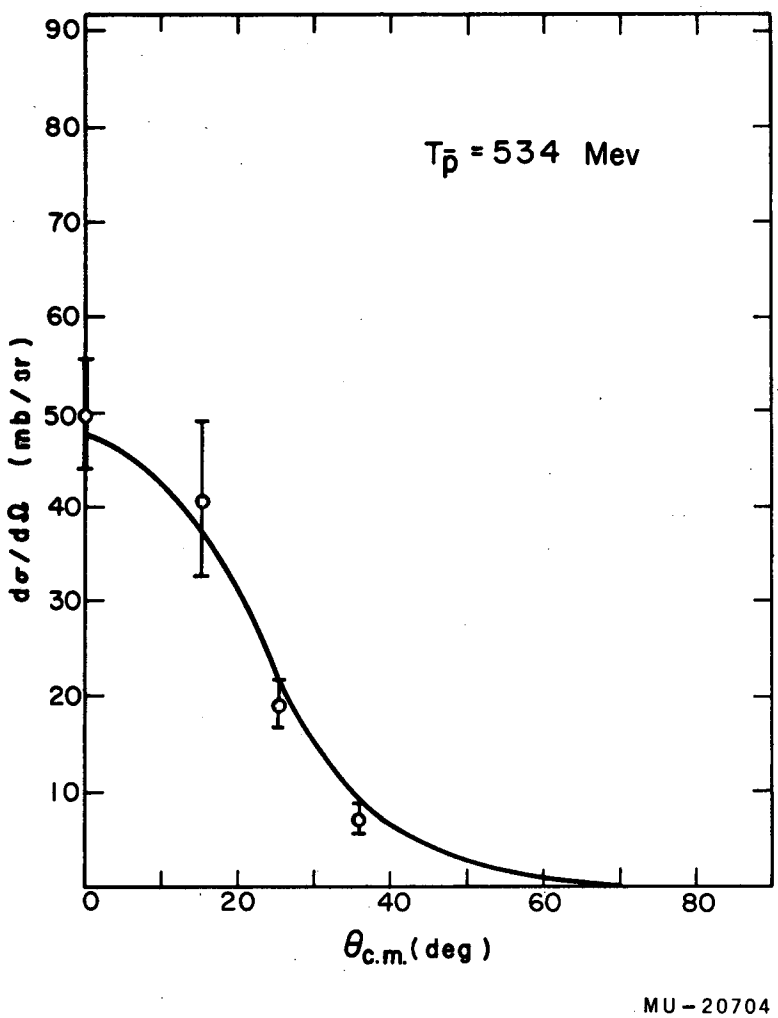

Fig. 14. Angular distribution of $\bar{p}$-p elastic scattering at 534 Mev.

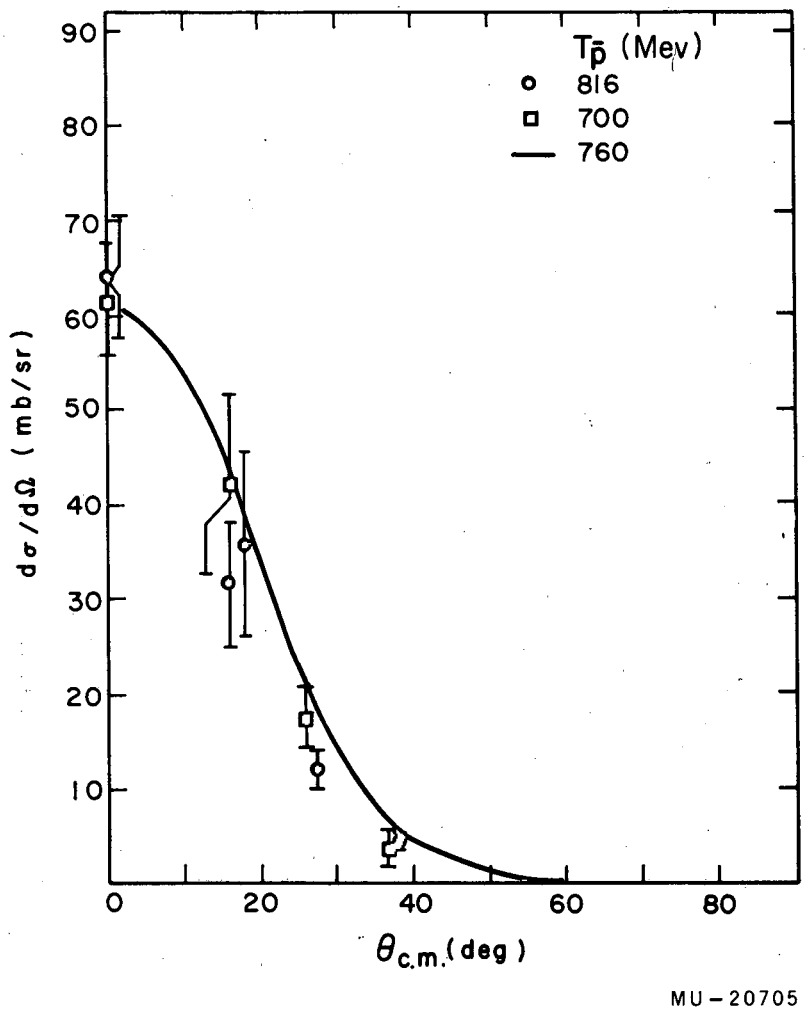

Fig. 15. Angular distribution of $\bar{p}$-p elastic scattering at 700 and 816 Mev.

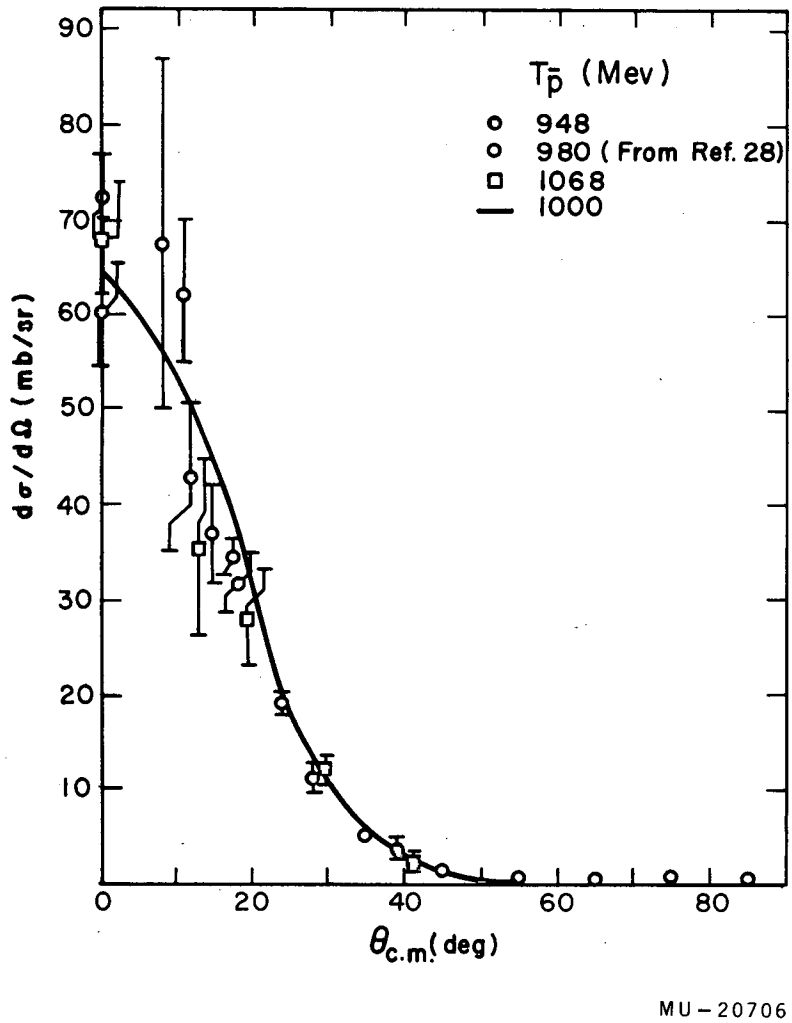

Fig. 16. Angular distribution of $\bar{p}$-p elastic scattering near 1 Bev.

The curves shown in Figs. 14, 15, and 16 were calculated by means of the optical model,[34] in which the scattering amplitude, diffraction cross section, and absorption cross section are given respectively by

$$f(\theta) = 1/\lambda\!\!\!^{-} \int_0^\infty (1-a)\, J_0\left(\frac{2}{\lambda\!\!\!^{-}}\, \rho \sin \theta/2\right) \rho d\rho \,, \tag{23}$$

$$\sigma_e = 2\pi \int_0^\infty |1-a|^2\, \rho d\rho \,, \tag{24}$$

$$\sigma_i = 2\pi \int_0^\infty (1-a^2)\, \rho d\rho \,. \tag{25}$$

For an incident wave of unit amplitude and zero phase, a is the amplitude and phase of the transmitted wave; ρ is of course the distance from the scattering center measured in a plane orthogonal to the incident-wave direction.

The particular ρ dependence of a used to fit data at 0.98, 1.25, and 2.0 Bev[24, 28] was

$$a = \begin{cases} 0 & \text{for } 0 < \rho \leqslant R_0 \,, \\ 1 - e^{-(\rho^2 - R_0^2)/\rho_0^2} & \text{for } \rho > R_0 \,. \end{cases} \tag{26}$$

This corresponds to a black region of total absorption which has radius R_0 surrounded by a region where the absorption decreases exponentially from R_0 with increasing ρ. Equations (23), (24), and (25) become, with the insertion of (26),

$$f(\theta) = \frac{R_0^{\,2}}{\lambda\!\!\!^{-}} \; \frac{J_1(x)}{x} + \frac{\rho_0^{\,2}}{2\lambda\!\!\!^{-}} \left\{ \exp\left[-(x')^2 + (x'')^2\right] - \sum_{n=1}^{\infty} \frac{1}{n!} (x'')^{2n} \left[\sum_{\ell=0}^{n-1} \frac{(-1)^{\ell}}{\ell!} (x')^{2\ell} \right] \right\}, \quad (27)$$

where

$$x = \frac{2R_0}{\lambda\!\!\!^{-}} \sin\theta/2, \; x' = \frac{\rho_0}{\lambda\!\!\!^{-}} \sin\theta/2 \; , \; x'' = R_0/\rho_0 \; ,$$

$$\sigma_e = \pi R_0^{\,2} + 1/2\, \pi\, \rho_0^{\,2} \; , \quad (28)$$

$$\sigma_i = \pi R_0^{\,2} + 3/2\, \pi\, \rho_0^{\,2} \; . \quad (29)$$

The values of the parameters R_0 and ρ_0 determined from the experimental cross sections appear in Table VIII. The values from Ref. 28 are also shown. To obtain these parameters, our cross sections at 700 and 816 Mev were averaged for the calculation at 758 Mev while those at 948 and 1068 Mev were combined to calculate the angular distribution at 1000 Mev. This was done because the angular distributions at these energies were nearly identical.

Table VIII

Optical-model parameters		
$T_{\bar{p}}$ (Mev)	R_0 (10^{-13} cm)	ρ_0 (10^{-13} cm)
534	0.95	0.93
758	0.95	0.87
1000	0.75	0.93
(980)[28]	0.73	1.03
(2000)[28]	0.57	0.98

Although the cross sections are approximately the same, a slight difference arises between the parameters of this experiment at 1000 Mev and those of Coombes et al.[24, 28] at 980 Mev. This is because we do not include the charge-exchange cross section as part of the absorption cross section in (29). As the charge-exchange cross section is small, there is no great change. The angular distribution curves of Figs. 14, 15, and 16 were calculated by means of (27), with the above parameters. Agreement with the experimental data is reasonably good. No special significance can be attached to such agreement, as the optical model can only attempt to describe qualitative features of high-energy elementary processes in a phenomenological manner. However, the results may be useful for comparisons that can be made with similar circumstances in the nucleon-nucleon case. We have taken the particular condition (26) because of its reasonable fit to the data of Armenteros et al.[28] at 980 Mev. Owing to our lack of information at large angles, a comparison between various density distributions is not feasible. It is shown, however, in Ref. 28, that conditions (26) give a much better fit to the data than a model of a completely gray region.

D. Conclusions

The $\bar{p}$-p cross sections determined by this experiment extend the experimental information on the $\bar{p}$-p interaction to nearly 1100 Mev. Prior information was known only to about 300 Mev. From Fig. 13 the obvious features are that the total $\bar{p}$-p cross sections remain nearly twice as large as the more familiar nucleon-nucleon cross sections of corresponding energy. Nearly 2/3 of the $\bar{p}$-p total cross sections are due to the annihilation phenomenon.

For the antiproton energy range of 50 to 250 Mev, the $\bar{p}$-p cross sections can be understood in terms of the theory of Ball and Chew.[5] Their model stresses the analogy between the antiproton-proton and the nucleon-nucleon systems. They use the Gartenhaus-Signell-Marshak potential,[35, 36] which seems to represent the nucleon-nucleon interaction up to about 200 Mev, and suitably modify it for the antinucleon case. The result is that a nucleon appears to an antiproton as a black hole or core region surrounded by a potential due to the pion cloud. The experimental data shown in Fig. 13 lend support to this model. In the energy range of applicability--i. e., 50 to 250 Mev--one finds $\sigma_e \approx \sigma_i \approx \sigma_t/2$. Thus the Ball-Chew model in its predictions is very nearly like a classical black-sphere region of size $\sim \lambda_\pi$ (pion Compton wave length). This is explained by the effectiveness of the outer potential due to the pion cloud in drawing the antiproton into the core region (the size of which is thought to be much less than λ_π), where it annihilates.

The methods used in the Ball-Chew calculations render them inapplicable in our energy range. However, a model along the same trend of ideas has been proposed by Koba and Takeda.[6] Their predictions are applicable at high energies and are in accordance with our measured cross sections. Their model is a completely phenomenological core region surrounded by a pion cloud. The core region is likened to a black sphere whose radius a_0 is left as an adjustable parameter.

Outside the core region is the potential due to the pion cloud, which they surmise can in principle be calculated by meson theory at high energies in a manner perhaps similar to that of Ball and Chew at low energies. It is expected that the pion potential will become less effective as one approaches high energies, and the annihilation cross section should become πa_0^2. This feature has also been pointed out by Chew.[10] Koba and Takeda considered the effect of the core region alone. As the classical approach is not valid in the energy region 300 to 800 Mev, they solve the Schrödinger equation and obtain for the annihilation cross section

$$\sigma_a = \pi (a_0 + \lambda\!\!\!^{-})^2 \tag{30}$$

instead of the classical result $\sigma_a = \pi a_0^2$. It is found that higher-order partial waves that classically would never reach the core can be partially absorbed, thus the absorption cross section is increased relative to the scattering cross section. Koba and Takeda find for $a_0 = 2/3\ \lambda\!\!\!^{-}_\pi = 0.94 \times 10^{-13}$ cm that the ratio of the elastic scattering cross section to the annihilation cross section is 1/2. From our experimental data in Fig. 13 one sees that σ_e/σ_i is 1/2 near 1 Bev and only slightly larger at 534 Mev. The experimental data (Fig. 13) for σ_i can very nearly be fitted by Eq. (30) for $a_0 = 0.95 \times 10^{-13}$ cm. For this value the high-energy points lie slightly above the curve, but this might be accounted for by a difference between σ_i and σ_a, because of meson production or inelastic scattering.

The optical-model analysis of the angular distributions of the elastic scattering also indicates a rather large opaque nuclear structure. In the region near 300 Mev, the differential scattering can be fitted by a completely black region of radius $\approx \lambda\!\!\!^{-}_\pi$.[17] In the proceding section it is seen that our data from 534 to 816 Mev can be fitted by a black region of radius $2/3\ \lambda\!\!\!^{-}_\pi$ surrounded by a region of decreasing grayness. Similar conditions exist to 2 Bev, as shown in Table VIII.

In view of the above observations it is probably not unreasonable to think of the $\bar{p}$-p interaction region as having a structure whose total size is $\sim \lambda\!\!\!^{-}_{\pi}$, within which the core region, where annihilation takes place, may be nearly as large as $2/3\ \lambda\!\!\!^{-}_{\pi}$. If the core region is indeed this large, the annihilation cross section must approach a constant 30 mb at very high energies. In general, theorists expect the core size to be of the order $\lambda\!\!\!^{-}_{\rho}$ (0.21×10^{-13} cm).[37, 38] The phenomenological impenetrable core regions of the Gartenhaus-Signell-Marshak and the Gammel-Thaler potentials used in the explanation of nucleon-nucleon interactions are of size $\lesssim 1/3\ \lambda\!\!\!^{-}_{\pi}$.[36, 39] Considering the close analogy to nucleon-nucleon scattering made by the Ball-Chew theory, the absorptive region in the antinucleon-nucleon case might be of comparable size. However, evidence from other types of high-energy experiments such as electron-proton scattering[40] indicate a root-mean-square charge radius of 0.77×10^{-13} cm. It is noticed that high-energy nucleon-nucleon and pion-nucleon experiments[25, 31, 41, 42] also suggest nearly opaque regions of radius $\approx 10^{-13}$ cm. While such analyses are not always taken too seriously, in view of the assumptions made, Tamm[43] has indicated that a large core region is not out of the realm of theoretical expectations. It should be of interest to explore the $\bar{p}$-p cross sections at energies beyond 3 Bev for information of this type.

VI. DETERMINATION OF ANTIPROTON-NEUTRON CROSS SECTIONS

A. Discussion

In order to attain a complete understanding of the antinucleon-nucleon system, information must be acquired not only for the $\bar{p}$-p interaction, but also for the $\bar{p}$-p (or $\bar{n}$-p). As in the nucleon-nucleon case, one can then determine the amount of interaction in each of the two possible isotopic spin (I) states of the antinucleon-nucleon system. The $\bar{p}$-n system is purely I = 1 state, while the $\bar{p}$-p system exists with equal probability in the I = 1 and I = 0 states. Tests for the validity of charge independence can thus be made from a knowledge of the $\bar{p}$-p and $\bar{p}$-n cross sections.

The experimental factors involved in the determination of the $\bar{p}$-p cross sections are considerably more attractive than those for the $\bar{p}$-n or $\bar{n}$-p cross sections. For the former, $\bar{p}$ beams exist, hydrogen targets are at hand, and both particles involved are charged. In the latter one is faced with the necessity of providing a neutron target or an antineutron beam, in addition to the difficult feature of detecting a neutral particle. The feasibility of obtaining antineutron beams utilizing the reaction $p + p \rightarrow \bar{n} + He^3$ was investigated;[44] the procedure was found very difficult. However, the use of antineutrons from the $\bar{p}$-p charge-exchange process seem to offer promise.[30]

The other alternative--which we have chosen here--is the indirect use of a neutron target via the deuteron. The hydrogen target used to obtain the $\bar{p}$-p cross sections in Section V was equally capable of containing deuterium, and a relatively ample supply of antiprotons was at hand. Thus in principle the subtraction of the $\bar{p}$-p cross sections from the $\bar{p}$-d cross sections could be made and values for the $\bar{p}$-n cross section assessed. To this end we have determined the $\bar{p}$-d cross sections at the same five energies as the preceding $\bar{p}$-p data. The $\bar{p}$-d data will be presented first as their validity seems secure (by virtue of the fact that they are ascertained in the same manner as the $\bar{p}$-p results. The subtraction procedure used for the $\bar{p}$-n values, which is subject to some uncertainty, is discussed in a subsequent section.

B. Antiproton-Deuteron Cross-Section Results

The various types of $\bar{p}$-d interactions--i.e. scattering, annihilation, etc.--were identified in the same manner as outlined in Sec. III. Calculation of the cross sections and correction factors was performed by the methods already mentioned for the $\bar{p}$-p cross sections. The results are listed in Table IX and plotted in Fig. 17.

No distinction can be made by our detection system between elastic $\bar{p}$-d scattering and quasi-elastic $\bar{p}$-p or $\bar{p}$-n scattering. Observations of the corresponding p^+d reaction at 660 Mev[45] indicate that the probability of the deuteron's remaining intact is quite small. It has therefore been assumed that the scatterings are all quasi-elastic. In the deuteron analysis no allowance has been made for the momentum distribution of the nucleons in the nucleus. Because of the predominant forward scattering, only about 20% of the scatterings are accompanied by a recoil nucleon that has sufficient energy to escape the target. For the runs made without lead converter there is some possible confusion between $\bar{p}$-p_d elastic scattering and the $\bar{p}$-p_d two-charged-pion annihilation mode, due to the deuteron internal momentum (p_d refers to the bound proton within the deuteron). Comparison of runs with and without converter has shown, however, that the effect is quite small and within the limits of our statistical errors. The difference between lead in and lead out also revealed no confusion between the majority of the elastic scatterings in which no recoil nucleon was detected and the $\bar{p}$-n_d one-charged-pion annihilation mode. This is principally because the one-charged-pion mode is expected to be somewhat rare. A low-energy experiment by Horwitz et al.[19] found only one event of this type in 34 $\bar{p}$-d annihilations. (It should be mentioned that the runs with and without the lead converter mentioned above were found to be statistically the same in most cases.) The results in Table IX represent all the data combined.

Table IX

$\bar{p}$-d cross sections (mb)				
$T_{\bar{p}}$ (Mev)	σ_t	σ_e	σ_i	σ_c
534	210 ± 5	80 ± 6	126 ± 5	3.3 ± 1.3
700	189 ± 5	67 ± 5	117 ± 4	5.4 ± 1.4
816	196 ± 6	78 ± 5	112 ± 4	6.5 ± 1.5
948	178 ± 5	71 ± 5	102 ± 4	4.4 ± 1.1
1068	184 ± 3	68 ± 4	109 ± 5	5.6 ± 1.0

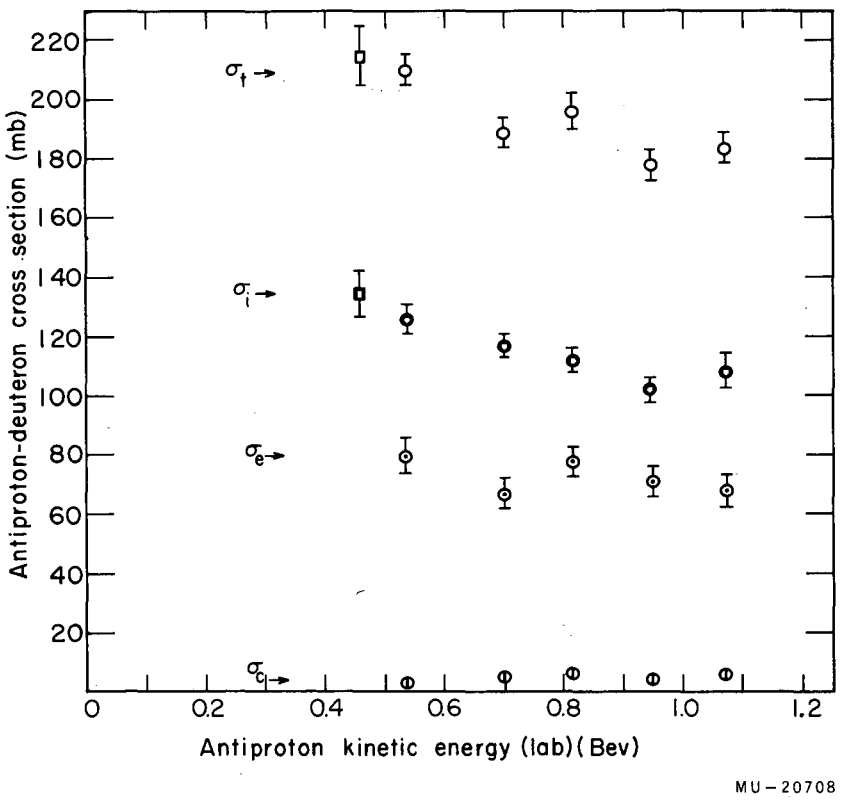

Fig. 17. Energy dependence of antiproton-deuteron cross sections.

An additional small correction to the elastic scattering may result from the meson-production process (sometimes referred to as inelastic charge exchange), $\bar{p} + n_d \rightarrow \bar{n} + n + \pi^-$. Judging from the magnitude of the cross section for similar processes (17) (18) in the $\bar{p}$-p case, one could not expect a correction of more than 4 or 5 mb.

From Fig. 17 it is seen that the energy dependence of the $\bar{p}$-d cross sections is very similar to that of the $\bar{p}$-p cross sections. The total and inelastic cross sections are 1.8 times the corresponding $\bar{p}$-p cross sections, while the factor for elastic scattering is approx 2.0. The charge-exchange cross sections are slightly smaller in deuterium. We recall that the charge-exchange process can occur only for the proton, consequently one might expect the same value for σ_c ($\bar{p}$-p) and σ_c ($\bar{p}$-d). However, the shadow correction discussed in the next section would reduce σ_c($\bar{p}$-d) relative to σ_c ($\bar{p}$-p), as is observed.

The only other existing data for the $\bar{p}$-d reaction (obtained by Chamberlain et al.[5]) have also been plotted in Fig. 17. They have measured σ_i and the total cross section in poor geometry with a cutoff angle (lab) of 14 deg. As their value of $\sigma_t^{14^o}$ = 174 mb is within 3 mb of our value for $\sigma_t^{13.2^o}$, we assume that the elastic scattering at 534 and 457 Mev is the same, and thus we obtain an additional value of the total cross section from their data at 457 Mev.

C. The "Eclipse" Effect and Antiproton-Neutron Cross Sections

To introduce this section we refer again to the analogous circumstance in the nucleon-nucleon system. Experimental information on nucleon-deuteron and nucleon-nucleon cross sections at high energies ($\approx$ 1 Bev) show that the sum of free-nucleon cross sections is approximately 10% greater than the deuteron cross section. Since the deuteron is a rather loosely bound structure, it is conceivable that at high energies (where $\lambda_{incident} << \sqrt{\frac{\sigma_i}{\pi}}$) the free-neutron and free-proton cross sections might be additive. However, it is found that a quantitative expression for the deuteron cross section, where x is the incident particle, must be written as

$$\sigma(x, d) = \sigma\ (x, p) + \sigma\ (x, n) - C\ , \tag{31}$$

where C is a correction factor sometimes called the "eclipse" or the "shadow" factor. This correction is due to the partial shielding of one nucleon by the other within the deuteron.

The shadow factor was first studied in detail by Glauber.[46] By means of diffraction theory Glauber has calculated a general expression for C in terms of the outgoing-wave amplitudes and phases. In view of the lack of knowledge of these factors, Glauber develops an approximate formula for the correction factor of the total cross sections,

$$C_t = 4\pi/k^2\ \mathrm{Re}\ \left\{ f_p(0)\ f_n(0) \right\} \left\langle r^{-2} \right\rangle_d\ , \tag{32}$$

where f(0) refers to the forward scattering amplitude, r is the neutron-proton separation, and the angular parentheses refer to an average value in the deuteron ground state. The result of (32) is very similar to what one would obtain by a simple classical computation of the decrease of incident flux when one nucleon is on front of the other; however, the work of Glauber differs in that the coherent diffraction scattering of the two nucleons is taken into account. One of the approximations made for the

particular expression (32) is that r is larger than the nucleon-interaction range. Under the additional assumption of a purely absorptive interaction, Glauber obtains, for the total deuteron cross section,

$$\sigma_t(x,d) = \sigma_t(x,p) + \sigma_t(x,n) - \frac{1}{4\pi}\,\sigma_t(x,p)\,\sigma_t(x,n)\,\left\langle r^{-2}\right\rangle_d . \qquad (33)$$

For the absorption cross section the relation

$$\sigma_i(x,d) = \sigma_i(x,p) + \sigma_i(x,n) - \frac{1}{2\pi}\,\sigma_i(x,p)\,\sigma_i(x,n)\,\left\langle r^{-2}\right\rangle_d \qquad (34)$$

is found. A similar expression for the scattering cross section can also be determined.[46]

To calculate the last term in the last two equations, the deuteron wave function must be known. Three different wave functions corresponding to a square-well potential, a Hulthén potential, and an attractive potential with a hard core were used to estimate $\sigma_t(\pi^- d)$. The respective results for the last term in (33) were 4.2, 5.3, and 3.3 mb.[47] The experimental result in the pion energy range 0.79 to 1.5 Bev was found to be 6±2 mb. For the nucleon-deuteron interaction near 1 Bev, the three wave functions above yielded correction factors of 5.7, 7.2, and 4.5 mb respectively.[48] Experimentally, the correction was found to be 7.4 mb. Thus for the particular cases mentioned the Glauber correction seems adequate. In addition it is noticed that the Hulthén wave function yielded the closest agreement in both of the above cases.

Considerations of the same corrections in the circumstance where the incident particle is an antiproton result in extremely large shadow factors. This is due to the large size of the $\bar{p}$-p (and presumably the $\bar{p}$-n) cross sections in relation to the nucleon-nucleon cross sections. The validity of the approximate Glauber formulas (33) and (34) is in serious doubt, especially in view of the assumption that the radius of interaction is much smaller than the size of the deuteron.

Blair has calculated the shadow effect by means of a semiclassical model[49] which does not use this last assumption mentioned above. It is therefore certainly more appropriate in the antinucleon case. Blair indicates the equivalence of his calculations to the Glauber result, and Keller[50] has shown that Blair's correction factor in practice is the same as the more general Glauber results. For small values of the free-nucleon cross sections the Blair calculations yield the same results as the approximate Glauber factors, and hence the same agreement for the πd and p^+d cross sections mentioned in the previous paragraphs. The disagreement with the approximate formulas becomes strongly apparent when the free-nucleon cross sections are 60 mb or greater, as is the case of antinucleons. The Blair calculations rest principally on the assumptions that the impulse approximation is valid and that the interaction can be represented by a black disc. These calculations were made in anticipation of $\bar{p}$-d cross sections such as ours.

In Table X the Blair correction factors for the inelastic or absorption cross sections are shown. The model for the deuteron used was the Hulthén wave function,

$$\psi_d = \left[\frac{\alpha}{2\pi} \frac{\beta(\alpha+\beta)}{(\alpha-\beta)^2}\right]^{1/2} \frac{\exp(-\alpha r)-\exp(-\beta r)}{r}, \qquad (35)$$

with $\beta = 6\alpha$, which corresponds to a triplet effective range of 1.75×10^{-13} cm. If a value $\beta = 7\alpha$ is used the correction factors are 2 mb larger. If the Gartenhaus wave function[51] was used the correction factors were found to be approx 2.5 mb smaller. Thus the correction factors are not extremely sensitive to the deuteron model used, as noted by Blair.

Table X

Evaluations of the $\bar{p}$-n cross sections (mb)

$T_{\bar{p}}$ (Mev)	$\sigma_i(\bar{p}\text{-}d)$	$\sigma_i(\bar{p}\text{-}p)$	"$\sigma_i(\bar{p}\text{-}n)$"	C_i	$\sigma_i(\bar{p}\text{-}n)$
534	126±5	70±3	56±6	23	79±6
700	117±4	66±3	51±5	20	71±5
816	112±4	63±3	49±5	19	68±5
948	102±4	56±2	46±4	17	63±4
1068	109±4	60±2	49±5	18	67±5

$T_{\bar{p}}$ (Mev)	$\sigma_t(\bar{p}\text{-}d)$	$\sigma_t(\bar{p}\text{-}p)$	"$\sigma_t(\bar{p}\text{-}n)$"	C_t	$\sigma_t(\bar{p}\text{-}n)$
534	210±5	118±6	92±8	27	119±8
700	189±5	116±5	73±7	23	96±7
816	196±6	108±5	88±8	24	112±8
948	178±5	96±3	82±6	20	102±6
1068	184±3	96±3	88±4	21	109±4

$T_{\bar{p}}$ (Mev)	$\sigma_e(\bar{p}\text{-}d)$	$\sigma_e(\bar{p}\text{-}p)$	"$\sigma_e(\bar{p}\text{-}n)$"		$\sigma_e(\bar{p}\text{-}n)$
534	80±6	42±5	38±8	[illegible]	40±10
700	67±5	42±4	25±7	[illegible]	25±8
816	78±5	38±4	40±7	[illegible]	44±9
948	71±5	33±3	38±6	[illegible]	39±7
1068	68±4	30±2	38±5	[illegible]	42±6

The correction factors for the total or elastic cross sections merit additional consideration. Shielding of the absorption cross section is more easily understood because absorptive processes by the two nucleons are mutually exclusive events. In the total cross section other factors are involved, such as interference effects, double scattering, and scattering by one nucleon followed by absorption by the other. It is shown by Glauber[46, 52] that all these effects are taken into account by his general correction formula for σ_t, of which (33) is an approximation. The difference between the formula for the total cross section (33) and the one for the absorption cross section (34) is simply a factor of 2. This difference is valid only for a purely absorptive interaction; however, it is independent of the opacity of the interaction region. (In view of the use of the optical theorem in conjunction with the last assumption to obtain (33), the resulting correction to the total cross section should be a minimum correction.) We therefore employ this factor of 2 together with the more explicit Blair results to obtain the total-cross-section corrections shown in Table X. The elastic $\bar{p}$-n cross section was obtained by subtracting σ_i from σ_t. The results are plotted in Fig. 18 for a comparison with the $\bar{p}$-p values from Fig. 13.

The fourth column of Table X, where the cross section is distinguished by quotation marks, is the apparent $\bar{p}$-n cross section. This is obtained by a direct subtraction of $\sigma(\bar{p}, p)$ from $\sigma(\bar{p}, d)$. The last column is the true $\bar{p}$-n cross section, where the correction factor (column 5) has been added to the apparent cross section.

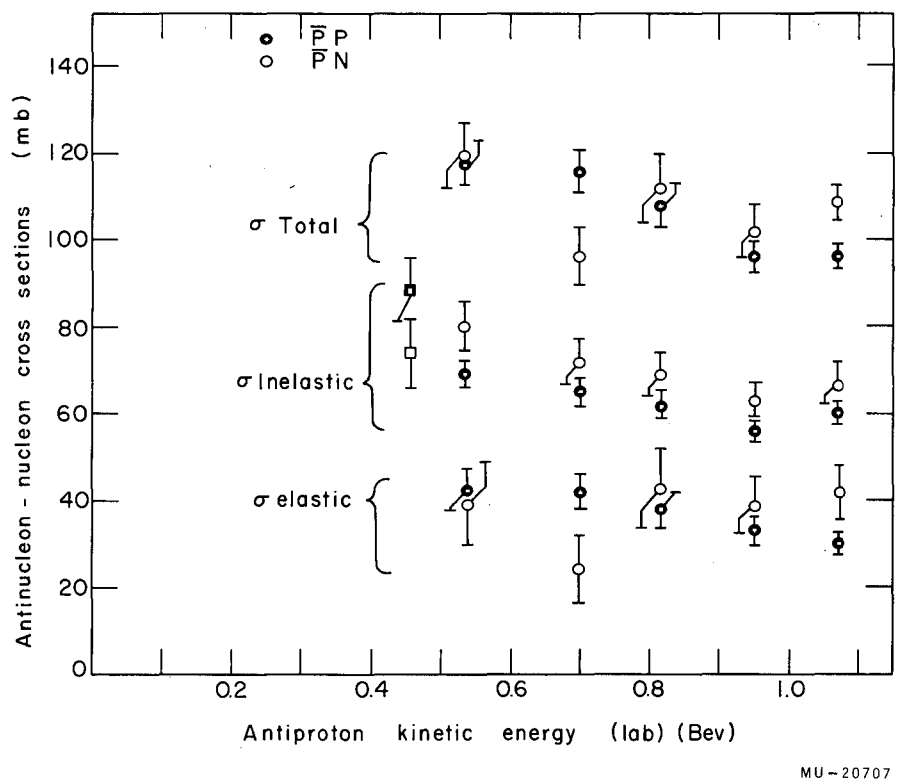

Fig. 18. Comparison of $\bar{p}$-p and $\bar{p}$-n cross sections in the energy range 450 to 1068 Mev.

D. Conclusion

From the presentation in Fig. 18 it is seen that the $\bar{p}$-n and the $\bar{p}$-p cross sections are statistically the same within the energy interval of this experiment. It should be emphasized that this conclusion, as well as the following ones, rests on the validity of the Blair correction factors employed to obtain the $\bar{p}$-n cross sections. These correction factors have not been experimentally proven for antinucleon cross sections as they have been for nucleon and pion cross sections. In view of the assumptions made in the derivations[46, 49] of the shielding factors, they are not expected to be entirely accurate, but to provide a reasonable estimate. The shadow correction to the annihilation cross sections seems the most reliable, because fewer assumptions are involved. The other shadow corrections would seem to be more uncertain because of the assumption of a purely absorptive interaction with zero phase shift.

The equality of $\bar{p}$-p and $\bar{p}$-n cross sections may not be totally unexpected. The near equality is noted in the calculations by Ball and Fulco[53] for antinucleons in the energy range 50 to 250 Mev. Their theoretical results are based on the theory of Ball and Chew.[5] As the low-energy experimental results for the $\bar{p}$-p cross sections support the theoretical expectations, it would not be surprising for the $\bar{p}$-n cross sections to do likewise, although no experimental $\bar{p}$-n information exists at low energies.

The $\bar{p}$-p system may interact through the isotopic spin states $I = 0$ and $I = 1$ with equal probability. The $\bar{p}$-n, however, exists only in the $I = 1$ state. Thus within the limits of our errors, the equality of the $\bar{p}$-n and $\bar{p}$-p cross sections reveals that the antinucleon-nucleon interaction occurs in the $I = 0$ and $I = 1$ states with the same probability. There exist inequality relations between $\bar{p}$-p and $\bar{p}$-n cross sections which are independent of detailed nuclear models and require only the charge independence of nuclear forces. These inequalities follow from the fundamental relations between the scattering amplitudes f_0 and f_1 between initial and final states of $T = 0$ and $T = 1$, which are

$$\sigma_e(\bar{p}, p) = \frac{1}{4} \left| f_0 + f_1 \right|^2 ,$$

$$\sigma_c(\bar{p}, p) = \frac{1}{4} \left| f_0 - f_1 \right|^2 , \tag{36}$$

$$\sigma_e(\bar{p}, n) = \left| f_1 \right|^2 .$$

The resulting expressions[54, 55, 56] are

$$\frac{d\sigma_c(\bar{p}-p)}{d\Omega} (0^o) \geqslant (k/4\pi)^2 \{\sigma_t(\bar{p}, n) - \sigma_t(\bar{p}, p)\}^2 , \tag{37}$$

$$\sigma_e(\bar{p}, p) + \sigma_c(\bar{p}, p) \geqslant 1/2\, \sigma_e(\bar{p}, n), \tag{38}$$

$$\left| \{\sigma_c(\bar{p}, p)\}^{1/2} - \{\sigma_e(\bar{p}, n)\}^{1/2} \right| \leqslant \{\sigma_e(\bar{p}, p)\}^{1/2} \leqslant \{\sigma_c(\bar{p}, p)\}^{1/2} + \{\sigma_e(\bar{p}, n)\}^{1/2} , \tag{39}$$

$$\left| \{\sigma_c(\bar{p}, p)\}^{1/2} - \{\sigma_e(\bar{p}, p)\}^{1/2} \right| \leqslant \{\sigma_e(\bar{p}, n)\}^{1/2} \leqslant \{\sigma_c(\bar{p}, p)\}^{1/2} + \{\sigma_e(\bar{p}, p)\}^{1/2} , \tag{40}$$

$$\left| \{\sigma_e(\bar{p}, n)\}^{1/2} - \{\sigma_e(\bar{p}, p)\}^{1/2} \right| \leqslant \{\sigma_c(\bar{p}, p)\}^{1/2} \leqslant \{\sigma_e(\bar{p}, n)\}^{1/2} + \{\sigma_e(\bar{p}, p)\}^{1/2} . \tag{41}$$

Relations (38), (39), (40), and (41) are all satified by our data of Fig. 18. The first relation (37) is satisfied by our values for σ_t and a value 6.5 mb/sr for the differential charge-exchange cross section obtained by Poirier et al.[30] The antinucleon-nucleon data are therefore consistent with the relations governed by charge independence in the energy range 500 to 1100 Mev. They are likewise in accordance with the predictions of Pomeranchuk[55] who has theorized that the $\bar{p}$-p and the $\bar{p}$-n cross sections should become equal at high energies as a consequence of conservation of isotopic spin. An additional theorem due to Pomeranchuk,[57] based on the dispersion relations for elastic scattering of nucleons in the forward direction, states that the $\bar{p}$-p and the p-p cross sections should be the same at high energies. At the energies under investigation here and at those of Ref. 28, the $\bar{p}$-p cross sections are much larger than the p-p cross sections. However, if the particular energy dependence of the antiproton cross sections (see Section V. D, Eq. (30)) noted here continues to higher energies, the antiproton cross sections may well approach the proton cross sections, which are very nearly a constant 40 mb from 2 to 6 Bev.[58]

ACKNOWLEDGMENTS

I wish to thank Professor Emilio Segrè for his interest and advice during the initial stages of the experiment. The foresight and advice of Professor Owen Chamberlain were welcomed throughout the course of the experiment. A large measure of credit for the work described in this paper belongs to Dr. Clyde Wiegand for his counsel and many contributions. The author is also grateful to Dr. Tom Ypsilantis and Dr. Herb Steiner for their participation in the experiment.

The author is indebted to Dr. Lewis Agnew for his help in erecting the magnetic channel, to Dr. Norman Booth for his aid in the successful operation of the experiment, and to Dr. Richard Lander for helpful discussions during the analysis. Thanks are also due Mr. Bill Johnson and Mr. Olav Vik, who gave their assistance in some of the initial preparations for the experiment.

A special note of appreciation is owing to Mr. Victor Brady for his help with the Ethelbert program, to Mr. Edwin McLaughlin for his design of the hydrogen target, and especially to Mr. Don Bliss and the Accelerator Technicians for their cooperation and helpfulness in the construction of many of the experimental components. Otto Smink deserves much of the credit for stabilizing the Turbo-encabulator.

The arduous task of scanning the oscilloscope film was performed by the enthusiastic efforts of Mr. Lennie Auerbach, Mr. Robert Bacastow, Mr. Jim Foote, Mr. Joe Lach, Mr. Ernest Rogers, and Mr. Hugh Rugge. Additional support in the scanning was given by Mr. Kirmach Nataini, Miss Jean Firby, Miss Frances Wilcox, and Mr. Robert Talsma. I am grateful to Miss Maureen Kane for her help in reducing the data.

Finally I wish to thank Mr. Harry Heard, Mr. Wendell Olsen, Mr. Bob Edwards, and Mr. Ken Stone and the entire Bevatron crew for their support and cooperation during the experimental run at the Bevatron.

This work was performed under the auspices of the U. S. Atomic Energy Commission.

APPENDIX

Antinucleon Cross-Section Formulas

In the determination of the $\bar{p}$-p total and partial cross sections, the experimental apparatus determines the following quantities:

I_0, the number of antiprotons entering the target,

I, the number of noninteracting antiprotons leaving the target,

I_e, the number of elastically scattered antiprotons,

I_i, the number of antiprotons that have inelastically scattered or annihilated,

I_c, the number of charge-exchange interactions,

where

$$I_0 = I + I_e + I_i + I_c \,. \tag{42}$$

For a very thin target, the above quantities immediately yield the cross section for the process in question. However, for a thick target, one must compensate for the number of antiprotons that annihilate in the target after they have scattered, for example.

First we recall the well-known formula for the rate of attenuation of the incident beam due to all processes

$$dI/_I = - \sigma_t \, dN, \tag{43}$$

where I is the intensity at any point in the target and σ_t is the total cross section. After the incident beam has traversed a thickness of N nucleons/cm^2, we have

$$I = I_0 \, e^{-\sigma_t N} \,, \tag{44}$$

where I_0 is the number of particles incident on the target.

In the case of the inelastic cross section, one must replace I in (43) by the amount of beam that is attenuated by inelastic processes (such as annihilation) alone,

$$\frac{dI_i}{I_0 - I_i} = - \sigma_i dN \,. \tag{45}$$

Thus we have

$$\sigma_i = \frac{1}{N} \ln\left(\frac{I_0}{I_0 - I_i}\right) . \tag{46}$$

This equation for the inelastic cross section is not always exact. In order for (46) to be valid, scattering must not decrease the path length for annihilation in the material. This is to say the target must be sufficiently large so that an elastic scattering near the frontend of the target does not cause the antiproton to immediately leave the material. In the preceding experiment, the target was 6 in. in diameter and the beam was of the order of 2 in. Scattering was found to be sharply peaked in the forward 20 deg (lab). In addition, the exit window was slightly rounded so that, in the first order, the path length for annihilation did not change even if the antiproton scattered. Further, it must be assumed that the annihilation cross section does not change greatly with energy, so that the cross section after scattering is approximately the same as before. The same type of analysis applies also to the charge-exchange process, although the magnitude of its effect is small owing to its small cross section. Therefore, the antineutron annihilation cross section is assumed to be the same as the antiproton annihilation cross section. The charge-exchange scattering is assumed to be predominantly forward. All these factors seem appropriate for the $\bar{p}$-p interaction in the energy range of this experiment.

In elastic scattering, ambiguities arise because the incident as well as the scattered $\bar{p}$ flux is decreased by annihilation and charge exchange. We find the number of antiprotons scattered (dI_e) in target thickness dN is

$$dI_e = \sigma_e I \, dN - \sigma_i I_e dN - \sigma_c I_e dN . \tag{47}$$

Rearranging and using (44), we have

$$\frac{dI_e}{dN} + (\sigma_i + \sigma_c) I_e = \sigma_e I = \sigma_e I_0 \exp(-\sigma_t N). \tag{48}$$

This first-order linear equation is readily integrable. (It is the same form as the equation for the activity of a two-element radioactive decay chain, which is found in most nuclear physics text.[59] The solution is

$$I_e = C \exp\left[-(\sigma_i+\sigma_c)\, N\right] + \exp\left[-(\sigma_i+\sigma_c)N\right] \int I_0 \sigma_e \exp\left[-(\sigma_t-\sigma_i-\sigma_c)N\right] dN \tag{49}$$

We note

$$\sigma_t = \sigma_i + \sigma_e + \sigma_c \,. \tag{50}$$

Therefore we can write (49) as

$$I_e = C \exp\left[-(\sigma_i+\sigma_c)\, N\right] + \exp\left[-(\sigma_i+\sigma_c)\, N\right] \int I_0 \sigma_e \exp\,(-\sigma_e N)\, dN \tag{51}$$

or

$$I_e = C \exp\left[-(\sigma_i+\sigma_c)N\right] + \exp\left[-(\sigma_i+\sigma_c)N\right]\left[-I_0 \exp\,(-\sigma_e N)\right] . \tag{52}$$

The constant of integration C is readily identified as I_0. We can now rewrite the last equation as

$$I_e = \left\{I_0 \exp\left[-(\sigma_i+\sigma_c)N\right]\right\} \left(1-\exp\,(-\sigma_e N)\right) . \tag{53}$$

The factor in braces is seen to be the attenuation of the incident beam due to inelastic processes and charge exchange. By definition we can write it as

$$I_0 \exp\left[-(\sigma_i+\sigma_c)N\right] = I_0 - I_i - I_c \,. \tag{54}$$

Substituting into (53), we have

$$I_e = (I_0 - I_i - I_c)\left[1-\exp\,(-\sigma_e N)\right] \tag{55}$$

Rearranging and using (42), we obtain

$$\sigma_e N = \ell n \left(\frac{I+I_e}{I}\right) . \tag{56}$$

The above formulas are idealized for a pure target material. In practice we have to consider the windows of the target container, which have cross section $\sigma_e{}^*$ and thickness N^*. Thus for a full target we actually measure

$$\sigma_e N + \sigma_e{}^* N^* = \ell n \left(\frac{I + I_e}{I} \right) , \tag{57}$$

and with target empty we measure

$$\sigma_e{}^* N^* = \ell n \left(\frac{I' + I'_e}{I'} \right) . \tag{58}$$

The usual subtraction yields the final formula for elastic scattering in terms of the immediate experimentally determined factors,

$$\sigma_e = \frac{1}{N} \ell n \left(\frac{I + I_e}{I} \times \frac{I'}{I' + I'_e} \right) . \tag{11}$$

Proceeding in the identical manner, we find the formula for the charge-exchange cross section is given by

$$\sigma_c = \frac{1}{N} \ell n \left(\frac{I + I_e + I_c}{I + I_e} \times \frac{I' + I'_e}{I' + I'_e + I'_c} \right) . \tag{12}$$

For completeness we note that, by the target-empty and target-full subtraction, (44) and (46) become

$$\sigma_t = \frac{1}{N} \ell n \left(\frac{I_0}{I} \times \frac{I'}{I'_0} \right) , \tag{9}$$

$$\sigma_i = \frac{1}{N} \ell n \left(\frac{I_0}{I_0 - I_i} \times \frac{I_0' - I_i'}{I_0'} \right) . \tag{10}$$

The last four formulas were used to determine the $\bar{p}$-p and $\bar{p}$-d cross sections.

REFERENCES

1. Chamberlain, Segrè, Wiegand, and Yspilantis, Phys. Rev. 100, 947 (1955).
2. E. Segrè, Annual Rev. Nuclear Sci. 8, 127 (1958).
3. E. Segrè, in Proceedings of the 1959 International Conference on Physics of High Energy Particles, Kiev, Russia.
4. O. Chamberlain, in Proceedings of the Seventh Annual Rochester Conference on High Energy Physics, Session X, 1957.
5. J. Ball and G. Chew, Phys. Rev. 109, 1385 (1958).
6. Z. Koba and G. Takeda, Progr. Theoret. Phys. (Kyoto) 19, 269 (1958).
7. Chamberlain, Keller, Mermod, Segrè, Steiner, and Ypsilantis, Phys. Rev. 108, 1553 (1957).
8. Cork, Lambertson, Piccioni, and Wenzel, Phys. Rev. 107, 248 (1957).
9. 1958 International Conference on High Energy Physics at CERN, B. Ferretti, Ed. (CERN, Scientific Information Service, Geneva, 1958), pages 107 and 108.
10. G. Chew, Proc. Acad. Sci. U.S. 45, 456 (1958).
11. Ref. 4, page X-6 .
12. Agnew, Chamberlain, Keller, Mermod, Rogers, Steiner, and Wiegand, Phys. Rev. 108, 1550 (1957).
13. Chamberlain, Keller, Segrè, Steiner, and Wiegand, Phys. Rev. 102, 1637 (1956).
14. Jackson, Dick A. Mack, and Clyde Wiegand, Beam Profile Indicator, UCRL-8386 Rev, Dec. 1958.
15. Clyde Wiegand, Cherenkov Counters in High-Energy Physics, UCRL-8148, Jan. 1958.
16. O. Chamberlain and C. Wiegand, Proceedings of the CERN Symposium on High Energy Accelerators and Pion Physics, Vol. II, (CERN, Geneva, 1956), p. 82.

17. Coombes, Cork, Galbraith, Lambertson, and Wenzel, Phys. Rev. 112, 1303 (1958).

18. Agnew, Elioff, Fowler, Lander, Powell, Segrè, Steiner, White, Wiegand, and Ypsilantis, Antiproton Interactions in Hydrogen and Carbon Below 200 Mev, Phys. Rev. 118, 1371 (1960).

19. Horwitz, Miller, Murray, and Tripp, Phys. Rev. 115, 472 (1959).

20. References D11, B5, and S1 in W. Hess, Revs. Modern Phys. 30, 368 (1958).

21. Batson, Culwick, Clepp, and Riddiford, 1958 International Conference on High Energy Physics at CERN, B. Ferretti, Ed. (CERN, Scientific Information Service, Geneva, 1958), p. 74.

22. Warren W. Chupp, Joseph S. Murray, and William A. Wenzel, Bevatron Targets, Beam Energy and Current Monitor Bevatron Internal Report (BEV-117), Feb. 27, 1956. (Additional information can be found in Bevatron Research and Development, UCRL-3444), June 1956.

23. Chamberlain, Chupp, Goldhaber, Segrè, Wiegand, Amaldi, Baroni, Castagnoli, Franzinetti, and Manfredini, Nuovo cimento 3, 462 (1956).

24. Charles Coombes (Lawrence Radiation Laboratory) private communication.

25. W. Rarita, Phys. Rev. 104, 222 (1956).

26. Bipin R. Desai, Pion Multiplicity in Nucleon-Antinucleon Annihilation, UCRL-9024 Rev, May 1960.

27. Emulsion results from many authors compiled by Baroni et al., Nuovo cimento 12, 564 (1959).

28. Armenteros, Coombes, Cork, Lambertson, and Wenzel, Antiproton-Proton Cross Sections at 1.0, 1.25, and 2.0 Bev, submitted to Phys Rev.

29. Button, Elioff, Segrè, Steiner, Weingart, Wiegand, and Ypsilantis, Phys. Rev. 108, 1557 (1957).

30. Poirier, Moyer, Hinrichs, Parker, and Carroll (Lawrence Radiation Laboratory), unpublished results. Values for σ_c and $d\sigma_c/d\Omega(0)$ given by J. Poirier in invited paper of April 1960 meeting of the American Physical Society.

31. Fowler, Shutt, Thorndike, Whittmore, Cocconi, Hart, Block, Harth, Fowler, Garrison, and Morris, Phys. Rev. 103, 1493 (1956).

32. W. A. Wallenmeyer, Phys. Rev. 105, 1058 (1957).

33. Goldhaber, Fowler, Goldhaber, Hoang, Kalogeropolous, and Powell (Lawrence Radiation Laboratory), unpublished results.

34. Fernbach, Serber, and Taylor, Phys. Rev. 75, 1352 (1949).

35. S. Gartenhaus, Phys. Rev. 107, 291 (1957).

36. P. Signell and R. Marshak, Phys. Rev. 109, 1229 (1958).

37. Yennie, Levy, and Ravenhall, Revs. Modern Phys. 29, 144 (1957).

38. Geoffrey Chew, Ref. 9, page 106.

39. J. Gammel and R. Thaler, Phenomenology of the Nucleon-Nucleon Interaction, Los Alamos Scientific Laboratory Report.

40. R. Hofstadter, Revs. Modern Phys. 28, 214 (1956), and Phys. Rev. 103, 1454 (1956).

41. Cork, Wenzel, and Causey, Phys. Rev. 107, 859 (1957).

42. Walker, Hushfar, and Shepard, Phys. Rev. 104, 526 (1956).

43. I. E. Tamm, Soviet Physics--JEPT 5, 154 (1957).

44. Burton J. Moyer, in Physics Division Semiannual Report, Aug. 1959, p. 33, UCRL-8936.

45. Meshcheriakov, Bogachev, leksin, Naganov, and Piskarev, in Proceedings of the CERN Symposium on High Energy Accelerators and Pion Physics, Vol. II, (CERN, Geneva, 1956), p. 124.

46. R. Glauber, Phys. Rev. 100, 242 (1955).

47. Cool, Piccioni, and Clark, Phys. Rev. 103, 1082 (1956).

48. Chen, Leavitt, and Shapiro, Phys. Rev. 103, 211 (1956).

49. J. S. Blair, University of Washington, Deuteron Cross Sections for High-Energy Projectiles (preprint).

50. Donald Keller, Nuclear Interactions of Antiprotons (thesis), UCRL-3855, July 1957, p. 53.

51. S. Gartenhaus, Phys. Rev. 100, 900 (1955).

52. R. Glauber, Lectures in Theoretical Physics (Interscience Publishers, New York, 1959), p. 378.

53. J. Ball and J. Fulco, Phys. Rev. 113, 647 (1959).

54. B. Malenka and H. Primakoff, Phys. Rev. 105, 338 (1957).

55. I. Pomeranchuk, Soviet Physics--JEPT 3, 306 (1956).

56. D. Amati and B. Vitale, Nuovo cimento 4, 145 (1956).

57. I. Pomeranchuk, Soviet Physics--JEPT 7, 499 (1958).

58. W. Hess, Revs. Modern Phys. 30, 368 (1958).

59. E. Fermi, Nuclear Physics (University of Chicago Press, Chicago, 1955), p. 24.

This report was prepared as an account of Government sponsored work. Neither the United States, nor the Commission, nor any person acting on behalf of the Commission:

A. Makes any warranty or representation, expressed or implied, with respect to the accuracy, completeness, or usefulness of the information contained in this report, or that the use of any information, apparatus, method, or process disclosed in this report may not infringe privately owned rights; or

B. Assumes any liabilities with respect to the use of, or for damages resulting from the use of any information, apparatus, method, or process disclosed in this report.

As used in the above, "person acting on behalf of the Commission" includes any employee or contractor of the Commission, or employee of such contractor, to the extent that such employee or contractor of the Commission, or employee of such contractor prepares, disseminates, or provides access to, any information pursuant to his employment or contract with the Commission, or his employment with such contractor.